A dual-mesh hybrid Reynolds-averaged Navier-Stokes/Large eddy simulation study of the buoyant flow between coaxial cylinders

DOI:
10.1016/j.nucengdes.2022.111789
https://doi.org/10.1016/j.nucengdes.2022.111789

Nuclear Engineering and Design 393 (2022) 111789
https://doi.org/10.1016/j.nucengdes.2022.111789

A dual-mesh hybrid RANS-LES study of the buoyant flow between horizontal coaxial cylinders

A.E.A. Ali[1], I. Afgan[2,1], D. Laurence[1] and A. Revell[1]

[1]Department of Mechanical, Aerospace and Civil Engineering, University of Manchester, George Begg Building, Sackville Street, Manchester M13 9PL, UK

[2]Department of Mechanical Engineering, College of Engineering, Khalifa University, Abu Dhabi, P.O. Box 127788, UAE

abdelmagid.emadabdelmagidali@manchester.ac.uk

Abstract

This study is concerned with the investigation of suitability of the dual-mesh method for buoyancy driven flow inside a cylindrical annulus of concentric cylinders. The buoyant force in this type of flow is generated by the temperature difference between the inner and outer cylinders. The dual-mesh approach is a hybrid RANS-LES method in which a RANS and an LES are run simultaneously on two different grids. In this approach, a criterion is used to determine the locations at which each simulation is expected to perform better than the other. Consequently, at every location the less accurate simulation is forced and corrected towards the more accurate one. It is observed that the lengthscale resolution criterion of Ali et al. (2021) behaves satisfactorily in defining the regions where the LES is corrected towards the RANS and vice versa. Moreover, both quantitative and qualitative analyses of the results are presented in order to show that the dual-mesh method has the potential to yield results that are better than the results of the pure RANS and the pure coarse LES simulations.

1. Introduction

The buoyant cylindrical annuli flow occurs in a number of engineering applications, one of which is the boiler penetration cavities of gas cooled nuclear power stations. In these cavities, there are pipes that carry a fluid from and into the boiler. Since the inner pipes contain colder fluid, natural convection occurs in the cavities, and eventually stratifies which may be damaging to the outer cylindrical cavity casing. Other applications relevant to this flow include solar collectors and cooling of high-voltage cables.

The cylindrical annuli configuration found in most of the studies in the literature has only one inner cylinder. The buoyancy driven flow in the boundary layer of the inner cylinder forms a plume that rises or falls (depending on whether the inner cylinder is hotter or colder than the outer cylinder) and impinges on the outer cylinder. The term "cylindrical annuli flow" is more general than the term "coaxial cylinders flow". The latter can be used for cases where the inner and outer cylinders have the same axis.

The study of Kuehn & Goldstein (1978) was one of the earliest studies of the annuli flow. Their experiments were conducted for a radius ratio (outer cylinder radius to inner cylinder radius) of 2.6 and over the $Ra = 2.2 * 10^2$-$7.7 * 10^7$ range (Ra is the Rayleigh number). It was found that at Ra numbers of the order of 10^5, instabilities in the region of the plume arise, eventually developing into turbulence as Ra is further increased.

Bishop (1988) and McLeod & Bishop (1989) examined experimentally the flow problem for a Ra between $8 * 10^6$ and $2 * 10^9$, expansion numbers between $0.25 - 1.0$ and a radius ratio of 4.85. A correlation linking the heat transfer rate to all the studied parameters was proposed. The time series of the temperature at a point located approximately at the mid of the gap between the cylinders at the 0° position (see Fig. 1) was analysed. This analysis showed that for an expansion number ($\beta\Delta T$) of 0.25 (where ΔT is the temperature difference between the two cylinders), high amplitude and low frequency laminar oscillations occured for the Ra numbers in the range of 10^7 and 10^8. On the other hand, for the $Ra \approx 10^9$ and $\beta\Delta T \approx 0.25$ case, oscillations with lower amplitudes and a wider range of frequencies were observed, indicating a turbulent flow at the probed point. The time series of the temperature near the inner cylinder's boundary layer showed that the boundary layer is laminar and features weak or no fluctuations for the lower Rayleigh numbers. However, for $Ra \approx 10^9$, strong fluctuations with low frequencies were observed to start at 120°, eventually leading to turbulent at the location of 0°. Furthermore, for all the Rayleigh numbers, increasing the expansion number was found to promote turbulence-transition. In summary, these studies were focused mainly on measuring the mean temperatures, temperature fluctuations and the average heat transfer rates over the cylinders and provided an explanation of the flow patterns for different values of the Rayleigh and expansion numbers.

Char & Hsu (1998) studied the flow through coaxial cylinders at different Rayleigh numbers in the range $8.02 * 10^5$-$1.18 * 10^9$ for radius ratios ranging from 2.6 to 4.58 using two low-Reynolds RANS turbulence models. These models were the "linear eddy viscosity model" of Launder & Sharma (1974) and the "non-linear eddy viscosity model" of Craft et al. (1993). At the lowest Ra number (which corresponds to a laminar flow), good predictions of the Nusselt number (Nu) values along the two cylinders were obtained, despite the presence of an overprediction of Nu at the point at which the plume impinges on the outer cylinder. On the other hand, for the higher Ra values, the results of the radial temperature profiles showed that the non-linear model performs better than the linear model in the region of the rising plume. This is because at the downstream end of this region a flow impingement occurs and the Launder-Sharma model is known to overpredict the turbulence levels at locations of flow impingement (Craft et al., 1993). However, the non-linear model was designed to reduce the overprediction of the turbulence levels at regions of high strain rates. At the other radial lines, the accuracy of the temperature profiles returned by both the models was found to deteriorate as one moves away from the plume region where the models showed an overprediction of the temperature predictions.

Wall-resolved Large Eddy Simulation (LES) or Direct Numerical Simulation (DNS) such Wu et al. 2017a, Wu et al. 2017b, Wu et al. 2019, Benhamadouche et al. 2020 and Ahmed et al. 2020 are very expensive for high Reynolds and/or Rayleigh number flows as they require a very fine mesh in the near-wall regions in all three directions to resolve the turbulence structures. Nonetheless, Miki et al. (1993) used the LES approach to study annuli flow situations characterised by different radius ratios and different Rayleigh numbers the highest of which was $Ra = 1.18 * 10^9$. Their study concluded that the dissipation introduced by the subgrid-scale model has a strong dependence on the value of the Smagroinsky constant (C_s). Using a C_s value of 0.1 for the case with the highest Ra, reasonable predictions of the mean temperature profiles were obtained. However, some discrepancies in the prediction of the temperature fluctuations were observed. The need to use a low C_s value was also confirmed by the successful LES study of Addad (2004), who simulated the $Ra = 1.18 * 10^9$ flow with STAR-CD using $C_s = 0.04$. Addad (2004) also assessed the performance of different RANS models by comparing their results to the LES data he produced. Another LES study in the literature is the one by Padilla & Silveira-Neto (2005), who studied the turbulence transition in an annuli with a radius ratio of 2 using the dynamic Smagorinsky model.

The study of Addad et al. (2006) sheds some light on two flow situations with high turbulence levels. One of these situations occurs in an annuli with a radius ratio of 3.37 and the other at the internal cylinder at $Ra = 2.38 * 10^{10}$. The turbulence levels in this flow are significantly larger than the ones in the $Ra = 1.18 * 10^9$ flow in an annuli with a radius ratio of 4.85. Indeed, the size of the buoyant plume in the former is greater than that in the latter. Large turbulence levels were also observed in a $Ra = 2.38 * 10^{10}$ flow in the annuli of three internal cylinders.

Kenjereš & Hanjalić (1995) also examined the coaxial cylinders flow at different radius ratios and at Rayleigh numbers that correspond to both laminar and turbulent flows by solving a $k - \varepsilon - \theta^2$ system of equations in which low-Reynolds effects are taken into account. Results were compared to both experimental and LES data from the literature. The algebraic model of the turbulent heat flux was found to yield reasonable results in terms of flow pattern, agreement with heat transfer correlations, the mean temperature and its fluctuations.. The study also included some simulations of eccentric cylinders configurations.

Addad et al. (2015) performed a Quasi-Direct Numerical Simulation (QDNS) of the $Ra = 1.18 * 10^9$ flow in a coaxial cylinder configuration with a radius ratio of 4.85 using STARCCM+. This study was done using an unstructured polyhedral mesh that was locally refined in the active flow areas using an estimate of the Kolmogorov lengthscale from a precursor low-Reynolds $k - \varepsilon$ RANS computation. Results of the time averaged temperature and its variance showed a good agreement with the experimental results of McLeod & Bishop (1989). This QDNS study produced detailed flow and thermal data that can be used to validate the first and second moments predicted by lower order models (e.g. Hybrid RANS-LES and RANS).

The current work aims to test the performance of a new hybrid RANS-LES method called "the dual-mesh approach" in predicting the coaxial cylinders flow. Hybrid RANS-LES is a class of turbulence modelling approaches whose development was motivated by the huge computational costs associated with wall-resolved LES. Resolving the flow structures in the viscosity affected regions close to the wall requires the mesh to be fine enough not only in the wall-normal direction (which is the requirement of a low-Reynolds RANS treatment) but also in the other directions. The basic idea of Hybrid RANS-LES methods is that in these methods, a RANS model is relied upon to handle the near-wall regions and the LES approach is used to resolve the relatively large turbulence structures away from the walls, see Revell et al. (2020) for further details.

The dual-mesh approach was developed by Xiao & Jenny (2012). Tunstall et al. (2017) later suggested a number of improvements to the approach. Furthermore, the dual-mesh idea was extended to problems involving heat transfer by Tunstall (2016). Ali et al. (2021) used the dual-mesh approach to simulate a buoyant square cavity flow and provided guidance on how the approach can be used to predict buoyancy driven flows. Dual-mesh-related studies can also be found in Xiao et al. (2016), Lardeau et al. (2018), de Laage de Meux et al. (2015), Davidson (2019) and Nguyen et al. (2020).

The flow situation investigated here is the same as the one studied by Addad et al. (2015). The results of this work were validated against the available QDNS data. The fact that the benchmark data available for this test case is at a low Rayleigh number, makes it difficult to demonstrate significant computational savings by resorting to hybrid RANS-LES instead of the conventional LES. However, one of the aims of this study is to prove that the dual-mesh method can work successfully for this type of flow, with flow featuressuch as unsteadiness, transition to turbulence and the coexistence of turbulent and laminar zones in the flow domain. One also ought to take into account the automatic switching criterion for RANS corrections to LES and vice versa. Future studies can then focus on obtaining high fidelity data for annuli flows with high turbulence levels (such as the ones studied by Addad et al., 2006) and then use the dual-mesh approach to simulate these situations with a similar methodology to the one presented here.

This paper is organised as follows. Section 2 introduces the reader to the studied cylindrical annuli case. Section 3 familiarizes the reader with the dual-mesh approach. This section also touches on the choices made here for the RANS and the LES modelling as well as the discretization techniques. The results obtained using the standalone and the hybrid simulations are discussed in detail in Section 4. Finally, Section 5 presents the conclusions of this study.

2. The cylindrical annuli benchmark

The geometry of the coaxial cylinder configuration is shown in Fig. 1. It consists of two concentric inner and outer cylinders (with radiuses of R_i and R_0, respectively) separated by an annular gap of width L_{ref}=R_0-R_i, which is occupied by a fluid. The cylinders are assumed to be long enough to allow the flow to be homogeneous in the z-direction.

The inner cylinder was maintained at a constant temperature T_h higher than the constant temperature of the outer cylinder T_c. Periodic boundary conditions were used in the homogeneous z-direction which was set at a length of $1.035 * L_{ref}$ (following Addad et al., 2015). The temperature difference $\Delta T = T_h - T_c$ and the fluid properties were set to represent a flow Rayleigh number ($Ra = \frac{Pr g \beta \Delta T {L_{ref}}^3}{\nu^2}$) of $1.18 * 10^9$ and the fluid Prandtl number (Pr) of 0.688. The values of R_0 and R_i were chosen to give $\frac{R_0}{R_i} = 4.85$.

In this study, the coaxial cylinder flow was computed using coarse LES, unsteady RANS as well as dual-mesh hybrid RANS-LES simulations. The RANS grid contained 120*240*1 cells (120 cells radially, 240 cells circumferentially and 1 cell in the z direction). The grid was uniform in the circumferential direction but was refined towards the cylinders in the radial direction using a hyperbolic tangent (tanh) stretching function. The radial grid spacing near the cylinders was set at $0.00044 L_{ref}$. On the other hand, the LES grid had 80*116 *20 cells, which were clustered towards the cylinders in the radial direction and towards the 0° position in the upper half of the geometry (to properly capture the rising plume). The node clustering in the radial direction was accomplished using the tanh stretching function of **Pointwise** by specifying cell sizes of $0.00044 L_{ref}$ and $0.0104 L_{ref}$ near the inner and outer cylinders, respectively. This grid allows the LES to resolve the radial gradients near the inner cylinder but is too coarse to resolve them in the vicinity of the outer cylinder, see Fig. 2 for mesh details.

Regarding the refinement of the LES mesh in the circumferential direction, the tanh stretching function was utilised to allow the grid to expand between the 0° and the 30° positions. The size of the circumferential grid spacing at 0° was $0.02597 L_{ref}$ near the outer cylinder (and $0.00536 L_{ref}$ near the inner cylinder[1]), whereas at 30° a circumferential spacing of $0.0824 L_{ref}$ near the outer cylinder (and $0.01699 L_{ref}$ near the inner cylinder) was used. The number of cells in the circumferential direction in the region between 0° and 30° was specified as 18. On the other hand, between the 30° and 180° positions, the circumferential number of cells was chosen to be 40 and the circumferential spacing of these cells was uniform (this spacing was set equal to $0.0824 L_{ref}$ and $0.01699 L_{ref}$ near the outer and inner cylinders, respectively). The grid was mirrored in a way that makes it symmetric between the left and the right halves of the geometry in the xy plane. The LES grid was made non-uniform in the circumferential direction to allow the LES to capture the rising plume (which is relatively thin due to the low Rayleigh number) near the 0° location. However, the LES grid is too coarse in the tangential direction for the LES to properly resolve the turbulence structures near the outer cylinder at the positions between 30° and 330°. The LES resolution in the z-direction was deliberately kept under resolved to utilise the dual-mesh approach.

[1] At a particular angular position, the circumferential grid spacing at the inner cylinder was calculated as $\frac{R_i}{R_0}$ times the circumferential spacing at the outer cylinder in order to obtain a high degree of mesh orthogonality.

3. Methodology

3.1. The dual-mesh approach

3.1.1. An overview of the approach

The dual-mesh approach is based on running simultaneous unsteady RANS and coarse LES simulations of the flow of interest. Here coarse LES represents an LES that is run on a grid that is not fine enough to resolve the near-wall flow structures but is sufficiently fine to properly resolve the turbulence structures away from the walls. Thus, in the near wall regions the coarse LES is corrected by the RANS, whereas far from the walls the RANS is corrected by the coarse LES.

In order to correct the two simulations towards each other, the RANS quantities are compared to the time-averaged LES quantities that are computed using an operation called the "Exponentially Weighted Averaging":

$$\langle\phi\rangle^{EWA}(t) = \int_{-\infty}^{t} \phi\,(t')\,\frac{1}{T_{avg}}\,exp\left(-\frac{(t-t')}{T_{avg}}\right)dt' \tag{1}$$

where ϕ is a time-dependent quantity which depends on the previous time levels (t'). Here T_{avg} is an averaging time scale and t represents the current time step values. We use a first-order approximation in time for the averaged value as

$$\langle\phi\rangle^{EWA,n} = (1-\alpha)\phi^{n} + \alpha\langle\phi\rangle^{EWA,n-1} \tag{2}$$

where $\langle\phi\rangle^{EWA,n}$ is the exponentially weighted average (EWA) of ϕ at the nth time step (or at the current level in time) and n-1 indicates the previous time step. The weighting factor α equals $\frac{1}{1+\frac{\Delta t}{T_{avg}}}$, where Δt represents the time step size, see Ali et al. 2021 for further details on weighted averaging. Comparing the RANS quantities to time-averaged LES quantities is one of the main differences between the dual-mesh approach and the single-mesh hybrid approaches since in the latter the space filtered LES variables and the RANS variables are matched. This gives the dual-mesh approach the advantage that it avoids "the grey area problem", which happens at locations where the solution transitions from "a RANS mode" to "an LES mode" in the early stages of separated shear layers with weak instabilities. These regions can feature a "grey area" characterized by low levels of both resolved and modelled turbulence (Mockett et al., 2015).

The LES velocity ($\overline{U_i}$) and temperature ($\bar{T}$) fields can be averaged using equation (2) to yield the averaged quantities $\langle\overline{U_i}\rangle^{EWA}$ and $\langle\bar{T}\rangle^{EWA}$, respectively. These quantities can be used to define resolved LES velocity and temperature fluctuations using the following equations

$$u_i'' = \overline{U_i} - \langle\overline{U_i}\rangle^{EWA} \tag{3}$$

$$t'' = \bar{T} - \langle\bar{T}\rangle^{EWA} \tag{4}$$

The LES velocity and temperature fluctuations along with the subgrid-scale (sgs) turbulent kinetic energy (k_{sgs}) and sgs temperature variance ($\overline{T'^2}_{sgs}$) can then be utilised to calculate the total LES EWA turbulent kinetic energy (k^{EWA}) and total LES EWA temperature variance (Θ^{EWA}) as

$$k^{EWA} = \langle 0.5\,u_i''\,u_i''\rangle^{EWA} + {k_{sgs}}^{EWA} \tag{5}$$

$$\Theta^{EWA} = \langle (t'')^2 + \overline{T'^2}_{sgs}\,\rangle^{EWA} \tag{6}$$

where ${k_{sgs}}^{EWA} = \langle k_{sgs}\rangle^{EWA}$. In the dual-mesh framework, in addition to making $\langle\overline{U_i}\rangle^{EWA}$ and $\langle\bar{T}\rangle^{EWA}$ consistent with the RANS velocity ($\langle U_i\rangle$) and RANS temperature ($\langle T\rangle$), respectively, one also aims to make k^{EWA} and Θ^{EWA} consistent with the RANS turbulent kinetic energy (k^R) and the RANS temperature variance ($\Theta^R = \langle T'^2\rangle$), respectively.

The RANS-LES consistency is achieved by adding source terms known as the "drift terms" to the momentum, temperature and turbulence equations of the RANS and the LES. The turbulence equations with drift terms include the equations of the RANS model, the k_{sgs} equation (which one needs to solve when using the one equation k

LES model) as well as the equations of the temperature variances $\overline{T'^2}_{sgs}$ and Θ^R. In the regions where the LES is corrected towards the RANS (which are called "the RANS regions"), the drift terms in the RANS equations are deactivated, whereas the drift terms in the LES transport equations are active which act to modify the transported variables in a way that drives the LES EWA variables towards their RANS counterparts. On the other hand, at locations where the RANS is corrected towards the LES (known as "the LES regions"), the LES drift terms are inactive, whereas the forcing terms in the RANS equations dervies the RANS quantities towards their corresponding LES EWA quantities.

3.1.2. Defining the RANS and the LES regions:

Previous dual-mesh studies in the literature utilize different methods for determining whether at a particular position, the RANS should drive the LES or vice versa. Xiao & Jenny (2012) specified a wall distance to separate the RANS and the LES regions. Later, Xiao et al. (2014) introduced an anisotropic definition of the integral lengthscale and used a lengthscale resolution criterion that compares the turbulence lengthscale in each direction with the grid size in the same direction. The LES regions were defined as the regions where the criterion indicates that the LES is well-resolved and the remaining locations were classified as the RANS regions.

Tunstall et al. (2017) defined a quantity called the LES zone weight (σ^L), which is equal to 1 in the LES regions but equals 0 in the RANS regions. Multiplying the LES drift terms by $(1-\sigma^L)$ ensured that the drift terms were deactivated in the LES regions and only remained active in the RANS regions. On the other hand, the RANS drift terms were controlled by multiplying them by the factor $(1-\sigma^R)$, where $\sigma^R = 1-\sigma^L$. The calculation of σ^L was based on the quantity $Re_y = \frac{\sqrt{k^R}y}{\nu}$, which is less than 200 in the viscosity affected regions and increases beyond 200 in the fully turbulent regions (see Andersson et al., 2011).

$$\sigma^L = 0.5\left(1 + \tanh\left(\frac{Re_y - 200}{10}\right)\right) \qquad (7)$$

Equation (7) is intended to return a σ^L profile in which σ^L is 0 close to the walls but reaches to 1 in the fully turbulent region. Equation (7) was successfully used by Tunstall (2016) and Tunstall et al. (2017) to determine the RANS and the LES regions in channel, periodic hill and T-junction flow configurations.

By simulating a buoyant square cavity flow, Ali et al. (2021) found that extra care needs to be taken when choosing a σ^L determining criterion for dual-mesh simulations of buoyant flows. This is because the square cavity features not only turbulent flow regions but also laminar regions and regions with low turbulence levels (these features are also present in the cylindrical annuli flow, as will be explained later in section 4). Hence, Re_y approaches 0 not only in the immediate wall vicinity but also in the laminar and the "weakly turbulent" regions. These regions include the core of the cavity and a significant part of the flow near the horizontal walls. Indeed, it has been observed that the equation (7) gives a σ^L behaviour in which σ^L is 0 in the core of the cavity. In addition, equation (7) was found to cause the region with $\sigma^L = 0$ near the horizontal walls to be thick. In cavities with perfectly conducting horizontal walls, the downstream ends of the horizontal walls feature the formation of an instability that causes a destabilization of the boundary layers near the vertical walls and enhances the turbulence levels in these boundary layers. Forcing the LES towards the RANS in a thick layer near the horizontal walls resulted in a significant damping of the LES instability, which caused the turbulence levels near the vertical walls to be low.

Another reason for avoiding a σ^L of 0 in laminar zones (such as the stratified and quasi-stagnant large core in the buoyant square cavity) is that in other than the classic Log-layer / viscous-sublayer interaction in isothermal boundary layer cases, the LES is often superior to the RANS in capturing intermittency and the destabilization of laminar zones by ejection of large-scale eddies. This effect is poorly modelled in RANS when closing triple moments and pressure-velocity correlations by turbulent diffusion of turbulence itself (a.k.a. turbulence transport terms and pressure diffusion in second moment closures). Thus, the RANS should be forced towards the LES in these regions.

For the computations, σ^L is estimated based on the ratio $\frac{{k_{sgs}}^{EWA}}{k^{EWA}}$ as shown below.

$$\sigma^L = \begin{cases} 1 & for\ \frac{{k_{sgs}}^{EWA}}{k^{EWA}} \leq 0.2 \\ 0 & for\ \frac{{k_{sgs}}^{EWA}}{k^{EWA}} > 0.2 \end{cases} \qquad (8)$$

This criterion was tested in the square cavity study reported of Ali et al. (2018) (see also Ali, 2020), and was found to lead to a sustainment of the turbulence levels and to give $\sigma^L = 1$ in the laminar regions. However, some clouds of cells with $\sigma^L = 0$ appeared within these LES regions. These cells are generally termed as "isolated cells" which

are undesirable in a hybrid RANS-LES computation (Xiao et al., 2014). Additionally, the studies of Xiao et al. (2014) and Davidson (2009) revealed some weaknesses of using the ratio of the averaged sgs turbulent kinetic energy to the total turbulent kinetic energy as an indicator of the LES resolution.

The weaknesses of the criterion based on $\frac{{k_{sgs}}^{EWA}}{k^{EWA}}$ encouraged Ali et al. (2021) to develop a criterion that considers the LES to be well-resolved wherever the grid size is smaller than the maximum of three different turbulence lengthscales. These scales need to be calculated a-priori from pure RANS simulation, before one runs the hybrid simulations as shown below

$$\sigma^L = \begin{cases} 1 & for\ \Delta \leq \max\left(\psi\lambda, \psi\frac{L_{RM}}{10}, 8C_{kolm}\eta\right) \\ 0 & for\ \Delta > \max\left(\psi\lambda, \psi\frac{L_{RM}}{10}, 8C_{kolm}\eta\right) \end{cases} \quad (9)$$

where Δ, L_{RM}, λ and η are the filter width, integral, Taylor and Kolmogorov lengthscales, respectively (these lengthscales are damped close to the wall using the functions ψ and C_{kolm}, which are defined later in (20) and (21)) using the following relationships

$$\Delta = (\Delta V)^{1/3} \quad (10)$$

$$L_{RM} = \frac{{k^R}_{Total}^{3/2}}{{\varepsilon^R}_{Total}} \quad (11)$$

$$\lambda = \sqrt{\frac{10\nu {k^R}_{Total}}{{\varepsilon^R}_{Total}}} \quad (12)$$

$$\eta = \left(\frac{\nu^3}{\{\varepsilon^R\}}\right)^{\frac{1}{4}} \quad (13)$$

Here ΔV is the cell volume, { } represents quantities that are averaged using a simple unweighted long time-averaging operation, ε^R is the modelled dissipation rate (obtained from the RANS dissipation equation) and ${k^R}_{Total}$ and ${\varepsilon^R}_{Total}$ represent the total kinetic energy and total dissipation rate of the fluctuating motions (which include both turbulent and mean flow related unsteady motions), respectively which are calculated as

$${k^R}_{Total} = \{k^R\} + {k^R}_{Res} \quad (14)$$

$${\varepsilon^R}_{Total} = \{\varepsilon^R\} + {\varepsilon^R}_{Res} \quad (15)$$

Where ${k^R}_{Res}$ and ${\varepsilon^R}_{Res}$ are the RANS kinetic energy of the resolved unsteady motions and its dissipation rate, computed as

$${k^R}_{Res} = 0.5 * \left\{{u_i}''^R\, {u_i}''^R\right\} \quad (16)$$

$${u_i}''^R = \langle U_i\rangle - \{\langle U_i\rangle\} \quad (17)$$

$${\varepsilon^R}_{Res} = 2\nu\left\{\langle S_{ij}\rangle\langle S_{ij}\rangle\right\} \quad (18)$$

$$\langle S_{ij}\rangle = 0.5\left(\frac{\partial\langle U_i\rangle}{\partial x_j} + \frac{\partial\langle U_j\rangle}{\partial x_i}\right) \quad (19)$$

Here ${u_i}''^R$ is the RANS resolved velocity fluctuation and $\langle S_{ij}\rangle$ is the RANS strain rate tensor. The third threshold $8C_{kolm}\eta$ in (9) is needed since the lengthscales $\psi\lambda$ and $\psi\frac{L_{RM}}{10}$ are not guaranteed to be large in all the laminar zones (even though they are based on ${k^R}_{Total}$ and ${\varepsilon^R}_{Total}$ and not on $\{k^R\}$ and $\{\varepsilon^R\}$). On the other hand, $8C_{kolm}\eta$ is highly likely to become large in these zones (because of the low values of ε^R) and thus serves to ensure that σ^L equals 1 in these regions. The near-wall damping of the Kolmogorov lengthscales introduced by C_{kolm} is necessary since in this region 8η becomes too large to represent the near-wall turbulence lengthscales. The definitions of ψ and C_{kolm} read as

$$\psi = \frac{3}{2}\left((1-\alpha^3)\varphi + \alpha^3\frac{2}{3}\right) \tag{20}$$

$$C_{kolm} = \begin{cases} 1 & for\ \mathrm{d} \geq \Delta_{max} \\ 0.3125 & for\ \mathrm{d} < \Delta_{max} \end{cases} \tag{21}$$

where $\varphi = \frac{\langle v^2 \rangle}{k}$ is the "wall-normal anisotropy", α is "the elliptic blending parameter" (these two quantities are solved for in the BL v2/k RANS model), d is the wall distance and Δ_{max} denotes the maximum local cell size. The use of a structured polar coarse LES grid here allows writing Δ_{max} as $\max(\Delta_r, \Delta_\theta, \Delta_z)$, where Δ_r, Δ_θ and Δ_z are the cell sizes in the radial, tangential and axial directions, respectively. The value 0.3125 in (21) was chosen to make $8C_{kolm}\eta$ equal to 2.5η close to the wall. This choice was inspired by Addad et al. (2015), who extracted the lengthscale η from a precursor RANS simulation and designed a very suitable QDNS grid by locally matching the grid size in specific directions to 2.5η.

The above lengthscale criterion was found to be less likely to cause isolated cells compared to the criterion in (8) and to perform satisfactorily for the square cavity flow. For further details about this new criterion, the reader is referred to Ali et al. (2021), where an explanation is provided for how the criterion was devised by taking into account some of the complex flow features that are commonly found in buoyant flows and by looking at the LES resolution criterions of Addad et al. (2008) and Uribe et al. (2010).

3.1.3. Equations of the cylindrical annuli flow in the dual-mesh framework

In this section, the equations that govern the flow studied in this work are reported. In these equations, the drift terms of the dual-mesh approach are included. Details about how the drift terms act to enforce the RANS-LES consistency can be found in Xiao & Jenny (2012), Tunstall (2016) and Ali et al. (2021). It should be noted that the dual-mesh framework used here is the modified framework of Tunstall (2016) (see also Tunstall et al., 2017). However, the LES zone weight σ^L was estimated using the lengthscale resolution criterion developed in Ali et al. (2021).

The effects of the density's dependence on temperature was modelled using the Boussinesq approximation. In this approximation, the density is taken to be variable in the gravity source term of the momentum equation but is assumed to be constant (equal to a value ρ_{ref}) in the other terms of the momentum, temperature and turbulence equations. Additionally, the variations of the other fluid properties are neglected.

The RANS and the LES momentum equations read, respectively as

$$\begin{aligned} \frac{\partial\langle U_i\rangle}{\partial t} + \langle U_j\rangle\frac{\partial\langle U_i\rangle}{\partial x_j} &= -\frac{1}{\rho_{ref}}\frac{\partial\langle p\rangle}{\partial x_i} \\ + \frac{\partial}{\partial x_j}\left((\nu+\nu_t)\left(\frac{\partial\langle U_i\rangle}{\partial x_j}\right)\right) & \\ + \left(1-\beta\left(\langle T\rangle - T_{ref}\right)\right)g_i & \\ + {Q_i}^R & \end{aligned} \tag{22}$$

$$\begin{aligned} \frac{\partial\overline{U_i}}{\partial t} + \overline{U_j}\frac{\partial\overline{U_i}}{\partial x_j} &= -\frac{1}{\rho_{ref}}\frac{\partial\overline{p}}{\partial x_i} \\ + \frac{\partial}{\partial x_j}\left((\nu+\nu_{sgs})\left(\frac{\partial\overline{U_i}}{\partial x_j}\right)\right) & \\ + \left(1-\beta\left(\overline{T} - T_{ref}\right)\right)g_i & \\ + {Q_i}^{L,u} + {Q_i}^{L,g} & \end{aligned} \tag{23}$$

where the RANS and the LES quantities are represented by the angle brackets $\langle\ \rangle$ and the overbar $\overline{\ }$, respectively. ρ_{ref} and $T_{ref} = \frac{T_h+T_c}{2}$ are the reference density and reference temperature, respectively. $\beta = \frac{1}{T_{ref}}$ represents the thermal expansion coefficient. ν_t and ν_{sgs} are the RANS eddy viscosity and the sgs viscosity, respectively. p and g_i are the pressure and the gravity vector, respectively. The drift terms in the above equations read as

$$Q_i^{L,u} = (1-\sigma^L)\left(\frac{\langle U_i\rangle - \langle \overline{U_i}\rangle^{EWA}}{\gamma_{l1}}\right) \tag{24}$$

$$Q_i^{L,g} = (1-\sigma^L)\left(\frac{G_i}{\gamma_{l2}}\right) \tag{25}$$

$$G_i = \left(1 - \frac{{k_{sgs}}^{EWA}}{k^{EWA}}\right)\frac{k^R - k^{EWA}}{k^R + k^{EWA}}\left(\overline{U_i} - \langle \overline{U_i}\rangle^{EWA}\right) \tag{26}$$

$$Q_i^R = \sigma^L \frac{\langle \overline{U_i}\rangle^{EWA} - \langle U_i\rangle}{\gamma_{r1}} \tag{27}$$

where the timescales γ_{l1}, γ_{l2} and γ_{r1} control the speed at which the solutions relax towards one another. The term Q_i^R forces the RANS velocity $\langle U_i\rangle$ towards the LES EWA velocity $\langle \overline{U_i}\rangle^{EWA}$ in the LES regions. On the other hand, in the RANS regions, the term $Q_i^{L,u}$ acts to correct the LES EWA velocity towards the RANS velocity. Furthermore, in these regions, in order to drive the LES EWA total turbulent kinetic energy k^{EWA} towards the RANS turbulent kinetic energy k^R, the resolved fluctuations of the LES velocity are modified using the term $Q_i^{L,g}$ and the modelled fluctuations are adjusted using a drift term $Q^{k_{sgs}}$ in the k_{sgs} equation, which reads as

$$\frac{\partial k_{sgs}}{\partial t} + \frac{\partial}{\partial x_j}\left(k_{sgs}\overline{U_j}\right) = 2\nu_{\text{sgs}}\overline{S_{ij}}^2 + \frac{\partial}{\partial x_j}\left(\nu_{sgs}\frac{\partial k_{sgs}}{\partial x_j}\right) - \frac{C_\varepsilon {k_{sgs}}^{3/2}}{\Delta} + G_{ksgs} + Q^{k_{sgs}} \tag{28}$$

$$\nu_{sgs} = C_k {k_{sgs}}^{1/2}\,\Delta\,\frac{\kappa}{C_\Delta}\left(1 - y\,exp\left(-\frac{y^+}{A^+}\right)\right) \tag{29}$$

$$\overline{S_{ij}} = 0.5\left(\frac{\partial \overline{U_i}}{\partial x_j} + \frac{\partial \overline{U_j}}{\partial x_i}\right) \tag{30}$$

$$Q^{k_{sgs}} = (1-\sigma^L)\frac{{k_{sgs}}^{EWA}}{k^{EWA}}\frac{k^R - k^{EWA}}{\gamma_{r2}} \tag{31}$$

where y is the wall distance and y^+ equals $\frac{y\sqrt{(\tau_w/\rho)}}{\nu}$, in which $\sqrt{(\tau_w/\rho)}$ represents the friction velocity. C_ε, C_Δ, A^+, C_k and κ are constants (see Table. 1). The buoyancy production term G_{ksgs} becomes simply $\beta g_i \frac{\nu_{sgs}}{Pr_{sgs}}\frac{\partial \overline{T}}{\partial x_i}$ when using the standard gradient diffusion hypothesis to model the sgs heat flux, which is present in the exact formulation of G_{ksgs}.

C_ε	C_Δ	A^+	C_k	κ
1.048	0.158	26	0.094	0.41

Table. 1. Constants of the "one equation k eddy viscosity model".

The forcing of the turbulent kinetic energy of the RANS k^R towards k^{EWA} in the LES regions is done by modifying the term that represents the generation rate of k^R in the turbulence equations of the RANS as

$$P_k = {P_k}^{model} + \sigma^L \frac{k^{EWA} - k^R}{\gamma_{r2}} \tag{32}$$

where P_k and ${P_k}^{model}$ are the modified and original generation rates, respectively. The relaxation time scales $\gamma_{l1}, \gamma_{r1}, \gamma_{l2}$ and γ_{r2} read as

$$\gamma_{l1} = \gamma_{r1} = max\left(C_{\gamma 1}\frac{k^R}{\varepsilon^R}, \Delta t\right) \tag{33}$$

$$\gamma_{l2} = \gamma_{r2} = max\left(C_{\gamma 2}\frac{k^R}{\varepsilon^R}, \Delta t\right) \tag{34}$$

where $C_{\gamma 1} = 0.1$, $C_{\gamma 2} = 0.01$ and ε^R is the RANS prediction of the turbulence dissipation rate.

The temperature equations of the RANS and the LES read, respectively:

$$\frac{\partial\langle T\rangle}{\partial t} + \langle U_j\rangle\frac{\partial\langle T\rangle}{\partial x_j} = \frac{\partial}{\partial x_j}\left(\left(\frac{\nu}{Pr} + \frac{\nu_t}{Pr_t}\right)\frac{\partial\langle T\rangle}{\partial x_j}\right) + Q^{\langle T\rangle} \tag{35}$$

$$\frac{\partial\overline{T}}{\partial t} + \overline{U_j}\frac{\partial\overline{T}}{\partial x_j} = \frac{\partial}{\partial x_j}\left(\left(\frac{\nu}{Pr} + \frac{\nu_{sgs}}{Pr_{sgs}}\right)\frac{\partial\overline{T}}{\partial x_j}\right) + Q^{\overline{T}} \tag{36}$$

where Pr_t (the turbulent Prandtl number) and Pr_{sgs} (the sgs Prandtl number) were set equal to 0.9 and 0.4, respectively. This lower value of Pr_{sgs} was found to improve the stability of the flow in the inner cylinder's boundary layer, which can become quite unstable because of the coarseness of the LES grid in the tangential direction. The stabilization results from the fact that lowering Pr_{sgs} adds more diffusion to the temperature field and is thus equivalent to adding some upwind. The drift terms $Q^{\langle T\rangle}$ and $Q^{\overline{T}}$ read

$$\begin{aligned} Q^{\overline{T}} &= (1-\sigma^L)\frac{\langle T\rangle - \langle\overline{T}\rangle^{EWA}}{\gamma_{l3}} \\ &+ (1-\sigma^L)\left(1 - \frac{\Theta^{EWA}{}_{sgs}}{\Theta^{EWA}}\right)\frac{\Theta^R - \Theta^{EWA}}{\Theta^R + \Theta^{EWA}}\frac{\overline{T} - \langle\overline{T}\rangle^{EWA}}{2\gamma_{l4}} \end{aligned} \tag{37}$$

$$\Theta^{EWA}{}_{sgs} = \langle\overline{T'^2{}_{sgs}}\rangle^{EWA} \tag{38}$$

$$\Theta^R = \langle T'^2\rangle \tag{39}$$

$$Q^{\langle T\rangle} = \sigma^L\frac{\langle\overline{T}\rangle^{EWA} - \langle T\rangle}{\gamma_{r3}} \tag{40}$$

where $Q^{\langle T\rangle}$ forces the RANS temperature $\langle T\rangle$ towards the LES EWA temperature, $\langle\overline{T}\rangle^{EWA}$ in the LES regions. The correction of the RANS temperature variance, Θ^R towards the LES EWA total temperature variance, Θ^{EWA} in these regions is achieved using the term $Q^{\langle T'^2\rangle}$ in the transport equation of the RANS variance (see (41)). On the other hand, the first part of the term $Q^{\overline{T}}$ forces the LES EWA temperature towards the RANS temperature in the RANS regions. Moreover, in these regions, the LES EWA total temperature variance is corrected towards the RANS temperature variance by adjusting the resolved temperature fluctuations (using the second part of $Q^{\overline{T}}$) and by modifying the modelled fluctuations using a source term $Q^{\overline{T'^2{}_{sgs}}}$ in the transport equation of the sgs temperature variance (see (42)). The equations of the RANS and the sgs temperature variances ($\langle T'^2\rangle$ and $\overline{T'^2{}_{sgs}}$) read as

$$\begin{aligned} &\frac{\partial\langle T'^2\rangle}{\partial t} + \langle U_j\rangle\frac{\partial\langle T'^2\rangle}{\partial x_j} = 2\frac{\nu_t}{Pr_t}\frac{\partial\langle T\rangle}{\partial x_i}\frac{\partial\langle T\rangle}{\partial x_i} \\ &-\frac{1}{R_t}\frac{\varepsilon^R}{k^R}\langle T'^2\rangle + \frac{\partial}{\partial x_j}\left(\left(\frac{\nu}{Pr} + \frac{\nu_t}{Pr_t}\right)\frac{\partial\langle T'^2\rangle}{\partial x_j}\right) \\ &+ Q^{\langle T'^2\rangle} \end{aligned} \tag{41}$$

$$\frac{\partial \overline{T'^2_{sgs}}}{\partial t} + \overline{U_j}\frac{\partial \overline{T'^2_{sgs}}}{\partial x_j} = 2\left(\frac{\nu}{Pr} + \frac{\nu_{sgs}}{Pr_{sgs}}\right)\frac{\partial \bar{T}}{\partial x_i}\frac{\partial \bar{T}}{\partial x_i} - \frac{1}{Pr}\frac{\varepsilon^L}{k_{sgs}}\overline{T'^2_{sgs}} + \frac{\partial}{\partial x_j}\left(\left(\frac{\nu}{Pr} + \frac{\nu_{sgs}}{Pr_{sgs}}\right)\frac{\partial \overline{T'^2_{sgs}}}{\partial x_j}\right) + Q^{\overline{T'^2_{sgs}}} \quad (42)$$

where R_t (the ratio of the thermal timescale to the mechanical timescale) was set equal to 0.5 and ε^L is the total LES dissipation rate, which can be obtained using:

$$\varepsilon^L = 2\nu\overline{S_{ij}}\,\overline{S_{ij}} + 2\nu_{sgs}\overline{S_{ij}}\,\overline{S_{ij}} \quad (43)$$

The drift terms in the temperature variance equations are defined as

$$Q^{\langle T'^2 \rangle} = \sigma^L \frac{\Theta^{EWA} - \Theta^R}{\gamma_{r4}} \quad (44)$$

$$Q^{\overline{T'^2_{sgs}}} = (1 - \sigma^L)\frac{\Theta^{EWA}{}_{sgs}}{\Theta^{EWA}}\frac{\Theta^R - \Theta^{EWA}}{\gamma_{l4}} \quad (45)$$

The relaxation time scales $\gamma_{l3}, \gamma_{r3}, \gamma_{l4}$ and γ_{r4} are defined as

$$\gamma_{l3} = \gamma_{r3} = max\left(R_t C_{\gamma 1}\frac{k^R}{\varepsilon^R}, \Delta t\right) \quad (46)$$

$$\gamma_{l4} = \gamma_{r4} = max\left(R_t C_{\gamma 2}\frac{k^R}{\varepsilon^R}, \Delta t\right) \quad (47)$$

3.2. Turbulence Models

The RANS and the LES models employed here were the BL v2/k model and the one equation k eddy viscosity model, respectively. Details about the models' equations and the treatments of the buoyancy and drift terms that were used to enhance the stability of the RANS model can be found in Ali et al. (2021). Further details on the models can also be found in Billard & Laurence (2012), Fureby et al. (1997) and Yoshizawa & Horiuti (1985).

3.3. Computational details

OpenFOAM 2.3.x was used to perform the simulations of this study. The dual-mesh simulations were performed using the same dual-mesh solver used in Ali et al. (2021), which was prepared by combining the dual-mesh code of Tunstall et al. (2017) with a buoyant solver in OpenFOAM called "buoyantBoussinesqPimpleFoam". As the name suggests, this solver models the effects of the density variation on the flow using the Boussinesq approximation. The thermal part of the dual-mesh method and the buoyancy specific terms in the turbulence models were also coded previously in OpenFOAM while conducting the study in Ali et al. (2021).

For both the RANS and the LES, the temporal discretization utilized second-order accurate backwards differencing scheme. The Courant number was kept less than 1 using OpenFOAM's adjustable time step option. For spatial discretization, the convection terms of the LES equations were handled using second-order central differencing. However, for the RANS, the second-order upwind scheme was used for the momentum equation, whereas the van Leer scheme of van Leer (1974) was employed for the remaining equations. The PISO algorithm (see Issa, 1986) was used to handle the pressure velocity coupling in both the RANS and the LES. The solver and the discretization procedures have been extensively tested and benchmarked over a variety of heat transfer and thermal hydraulics applications in the past, see Guleren et al. 2010, Han et al. 2012, Afgan et al. 2008, Abed & Afgan 2017, Abed & Afgan 2020, Abed et al. 2020a, Abed et al. 2020b, Abed et al. 2021 and Ali et al. 2021.

4. Results

In all the results shown here, the velocity vector ($\boldsymbol{U}$), radius (r) and temperature (T) were nondimensionalized in the following manner

$$\mathbf{U} = \frac{\boldsymbol{U}}{\sqrt{g\beta\Delta T L_{ref}}}, \mathrm{r} = \frac{(r - R_i)}{(R_0 - R_i)}, \mathrm{T} = \frac{(T - T_h)}{(T_c - T_h)} \qquad (48)$$

where g is the magnitude of the gravity vector and $\sqrt{g\beta\Delta T L_{ref}}$ represents a buoyant velocity scale. When estimating the second moments of the unsteady RANS and the LES simulations, both the resolved and the modelled components of the moments were taken into account. An explanation of this calculation can be found in Sebilleau (2016).

The averaging period of the LES in the dual-mesh simulation (T_{avg}) was set to to 41 $\frac{L_{ref}}{\sqrt{g\beta\Delta T L_{ref}}}$. This period was found to be long enough to yield smooth averaged fields; multiplying the averaging period by 2 had a almost no effects on the results.

Section 4.1 gives an overview of the results of the pure coarse LES and the pure unsteady RANS computations. In section 4.2, these results are discussed in more detail. In addition, the dual-mesh results obtained using the lengthscale criterion of equation (9) are also shown in section 4.2.

4.1. Results obtained from the standalone simulations:

As mentioned in the introduction, a challenging feature of this flow is the presence of a turbulence transition. This transition isimpossible to capture with a standard LES on a coarse grid similar to the one used here. Indeed, the one equation k model yields a non-zero k_{sgs} (and hence a non-zero ν_{sgs}, which is calculated from k_{sgs} using (29)) in the laminar boundary layer over the inner cylinder. The production term in equation (28), $2\nu_{sgs}\overline{S_{ij}}^2$ has a strain rate, which is relatively large near the inner cylinder's boundary layer (innerCBL) because of its small thickness (the large velocity gradients can be observed for example from Fig. 18-Fig. 20). Since the constant C_k used in the ν_{sgs} calculation is non-zero near the inner cylinder, the large strain rate causes a large k_{sgs} production term, which in turn causes a large ν_{sgs}. This causes a significant dissipation of the instabilities in the boundary layer, triggered by the gravity waves in the stably stratified bottom half of the annuli. The damping of these instabilities by a large ν_{sgs} delays the transition to turbulence of the buoyant plume. This late transition can be seen from Fig. 11 (a).

The dynamic Smagorinsky model (see Germano, 1992 and Lilly, 1992) was used in an attempt to overcome the transition delay problem experienced when using the one equation k model. The benefit of the dynamic model is that the dynamic procedure of the model yields a zero Smagorinsky constant in the laminar boundary layer and in turn a zero ν_{sgs} (see Afgan 2007 and Kahil et al. 2019 for further details on the laminar to turbulent transition models for LES). However, the vanishing ν_{sgs} in the innerCBL was observed to cause significant numerical instabilities since in this region the grid is coarse in the tangential direction (except at the locations close to the 0° position). Indeed, when the dynamic Smagorinsky model was used in a dual-mesh simulation, solution divergence was encountered. For this reason, the dynamic model was abandoned.

An alternative approach to improve the prediction of the turbulence transition in a dual-mesh simulation is to use the one equation k model and lower ν_{sgs} in the innerCBL and the initial stages of the plume (these regions cover the transitional flow region) to a value that is relatively small but non-zero. This can be done by lowering the constant C_k only in the cells where ν_{sgs} needs to be lowered and not altering its value at the remaining locations. A low value of C_k=0.0043 was found to be a suitable choice. However, instead of manually defining the region where $C_k = 0.0043$, an automatic identification procedure was used. This procedure was applied by first estimating the ratio $\frac{\{\mathrm{ksgs}\}}{\{\mathrm{kTotal}\}}$ (kTotal is the total turbulent kinetic energy, which includes a sgs contribution as well as a contribution from the resolved fluctuations) from the results of the pure coarse LES simulation in which $C_k$was set to 0.094 everywhere. This ratio is relatively large at the cells in the innerCBL because of the large k_{sgs} and the small values of the resolved variances of the velocity components (the resolved instabilities are damped due to the high ν_{sgs}). However, this ratio can also be significantly large near the outer cylinder if the grid is very coarse. One quantity that can be used with the ratio $\frac{\{\mathrm{ksgs}\}}{\{\mathrm{kTotal}\}}$ to distinguish the boundary layer over the inner cylinder from the outer cylinder's boundary layer (outerCBL) is the LES zone weight (σ^L) that is based on the lengthscale criterion (see (9))[2]. In the innerCBL, $\sigma^L = 1$ (see Fig. 6) and $\frac{\{\mathrm{ksgs}\}}{\{\mathrm{kTotal}\}}$ is large, whereas near the active flow regions of the outerCBL $\sigma^L = 0$ and $\frac{\{\mathrm{ksgs}\}}{\{\mathrm{kTotal}\}}$ can be large or small depending on the grid resolution. Consequently, C_k can be calculated as

[2] The behaviour of this criterion in the annuli flow is explained in section 4.2.

$$C_k = \begin{cases} 0.0043 & for\ \dfrac{\{ksgs\}}{\{kTotal\}} \geq 0.5\ and\ \sigma^L = 1 \\ 0.094 & otherwise \end{cases} \quad (49)$$

The above equation can be used to calculate C_k in the dual-mesh hybrid simulation. However, the hybrid simulation needs to be preceded by a coarse LES simulation for the purpose of calculating the $\frac{\{ksgs\}}{\{kTotal\}}$ ratio. A contour plot of C_k estimated using (49) is shown in Fig. 5. It can be observed from this figure that (49) correctly gives $C_k = 0.0043$ near the inner cylinder and in the initial stages of the plume (thus C_k is lowered in the transitional flow areas), whereas in the remaining regions, the C_k values are not lowered from their default value of 0.094.

In order to demonstrate that even with a good transition prediction the pure coarse LES cannot predict the flow near the outer cylinder correctly (due to the under-resolution of the grid in this region), a second coarse LES simulation was also run. In this simulation, the values of C_k calculated using (49) were utilised when calculating ν_{sgs} (using (29)) in order to obtain smaller values of ν_{sgs} near the inner cylinder compared to the ν_{sgs} values obtained in the previous coarse LES (with $C_k = 0.094$ everywhere). An improved transition prediction can be observed from the contours of the instantaneous and mean velocity magnitudes taken from the coarse LESs with default and reduced C_k values (Fig. 11 (a), Fig. 11 (b), Fig. 13 (a) and Fig. 13 (b)). The default C_k simulation predicts a plume that is thinner than the one in the reduced C_k simulation because the latter predicts an earlier transition, which allows the turbulence mixing to entrain more of the surrounding fluid into the plume. A quantitative comparison between the results of the two coarse LESs can be found in section 4.2.

A contour plot of the pure RANS mean velocity magnitude is presented in Fig. 13 (c). This simulation predicts a thin plume and a small thickness of the outerCBL. The thin plume prediction is an indication of insufficient turbulence levels. It can also be observed from the RANS turbulent kinetic energy contours (Fig. 14 (a)) that the RANS predicts a delayed transition compared to the reduced C_k LES simulation, which features turbulent flow structures in the vicinity of the inner cylinder (see Fig. 11 (b)). Fig. 14 (b) shows the kinetic energy of the resolved unsteady motions in the RANS simulation. The non-zero values of this parameter in the plume region are caused by the fact that the plume motion is unsteady. This unsteadiness is apparent in the snapshot of the RANS velocity shown in Fig. 12 (a).

The flow streamlines predicted by the different simulations are shown in Fig. 15. These streamlines show that the plume rises from the inner cylinder, impinges on the outer cylinder and then flows along this cylinder. As the hot plume is flowing along the outer cylinder against the action of gravity, the plume starts to decelerate. The effect of the deceleration is more pronounced on the outer edge of the plume compared to the near-wall jet, which is able to penetrate deeper along the outer cylinder. This is because the outer edge of the plume experiences more mixing with the fluid outside of the boundary layers than the near-wall jet. It can be seen that the fluid that forms the descending plume after being significantly decelerated by gravity moves slowly to fill the place of the fluid entrained by the rising plume and the innerCBL. It can also be observed that the fluid in the region below the inner cylinder flows at a very low velocity into the innerCBL. Indeed, this region is almost stagnant, featuring a stable stratification and is almost laminar.

4.2. Analysis of the dual-mesh results and a comparison with the results of the standalone simulations:

With Regards to the dual-mesh hybrid simulation, the criterion of Ali et al. (2021) was found to behave satisfactorily in defining the RANS and the LES regions. A contour plot of the LES zone weight (σ^L) estimated using this criterion is shown in Fig. 6. It can be observed that the RANS regions are mainly located in the vicinity of the outer cylinder. Furthermore, the criterion allows the flow field of the LES to develop without being forced towards the RANS in the innerCBL and in the plume region. These regions feature the formation of flow instabilities and modifying the LES fluctuations via the relaxation forcing in these regions can be dangerous as it can dampen these instabilities, which in turn might delay the occurrence of the turbulence transition.

The fact that the lengthscale resolution criterion causes the RANS to encounter a significant forcing towards the LES in the region with a strong RANS instability (in the plume region) leads to a destruction of the RANS instability, which makes the hybrid RANS simulation reach an almost steady-state, which can be observed from the instantaneous hybrid RANS velocity field shown in Fig. 12 (b). The steadiness of the RANS simulation facilitates setting up the dual-mesh simulation since in an unsteady RANS the averaging timescale (T_{avg}) of the LES is required to be much smaller than the RANS instability time scales as suggested by Xiao & Jenny (2012). A similar destruction of the RANS instability due to a significant forcing of the RANS was also observed in the study of Ali et al. (2021).

In order to explain the behaviour of the lengthscale criterion, contour plots of the different lengthscales in (9) are shown along with a number of radial profiles of the lengthscales and σ^L in Fig. 3, Fig. 4, Fig. 7 and Fig. 8. It can be observed from the profiles at 30^0 and 60^0 that the wall distance at which σ^L becomes 1 is determined by the location in the LES grid where Δ becomes smaller than the largest lengthscale among the lengthscales $\psi\frac{L_{RM}}{10}$, $\psi\lambda$ and $8C_{kolm}\eta$. Fig. 8 (c) shows that the lengthscale $8C_{kolm}\eta$ becomes large in nearly all the laminar regions, which include the stratified region at the bottom of the annuli and the initial stages of the plume (the lengthscales were calculated from the results of the pure RANS, which predicts a delayed plume turbulence transition). Fig. 9 shows the behaviour of the lengthscales $\frac{\psi}{10}\frac{\{k^R\}^{3/2}}{\{\varepsilon^R\}}$ and $\psi\sqrt{\frac{10\nu\{k^R\}}{\{\varepsilon^R\}}}$, which are based on turbulence quantities unlike the lengthscales $\psi\frac{L_{RM}}{10}$ and $\psi\lambda$ (the contours of which are shown in Fig. 8), which are calculated from quantities that include contributions that result from both turbulence and mean flow unsteadiness. It can be observed that the RANS predicts $\frac{\psi}{10}\frac{\{k^R\}^{3/2}}{\{\varepsilon^R\}}$ and $\psi\sqrt{\frac{10\nu\{k^R\}}{\{\varepsilon^R\}}}$ to be small in the region of the rising plume. If these lengthscales were used in the definition of the resolution criterion (equation (9)) instead of using $\psi\frac{L_{RM}}{10}$ and $\psi\lambda$, σ^L would have become 0 at some locations within the plume region. On the other hand, in this region $\psi\frac{L_{RM}}{10}$ and $\psi\lambda$ are larger than the grid size and using these lengthscales in the resolution criterion makes σ^L=1 in the entire region. Indeed, Fig. 3 (a) shows that at 0^0, $\psi\frac{L_{RM}}{10}$ and $\psi\lambda$ are greater than Δ except near the cylinders. However, the fact that $8C_{kolm}\eta$ even with the damping introduced by C_{kolm} is significantly larger than Δ in the vicinity of the inner cylinder makes σ^L equal to 1 in this region (the region where the damping introduced by C_{kolm} is active in the immediate vicinity of the inner cylinder can be seen in Fig. 8 (c) and in the profiles of the lengthscales shown in Fig. 3). The definitions of the lengthscales in (9) thus successfully ensure σ^L=1 at all the locations of the rising plume apart from the region near the outer cylinder.

The radial profiles of the lengthscales (Fig. 3) show that near the outer cylinder, the lengthscales $\psi\frac{L_{RM}}{10}$ and $\psi\lambda$ increase smoothly in the wall-normal direction. On the contrary, the profiles of the undamped lengthscales $\frac{L_{RM}}{10}$ and λ (Fig. 4) feature relatively large gradients near the outer cylinder. Similar observations of this unsmooth near-wall behaviour of the undamped lengthscales have been reported by Uribe (2010) and Ali et al. (2021) and were the reasons why the authors introduced near-wall lengthscale damping in their resolution criterions. Furthermore, it can be seen that near the outer cylinder, 8η is too large to represent the lengthscale of the turbulence structures, whereas the damped lengthscale $8C_{kolm}\eta$ gives a more reasonable estimation of the size of these structures. Another observation that can be made from Fig. 3 (b)-(d) is that the location outside of the near-wall region of the outer cylinder where $8C_{kolm}\eta$ intersects with the maximum of the lengthscales $\psi\frac{L_{RM}}{10}$ and $\psi\lambda$ shifts closer to the outer cylinder as θ (the angular location) increases. This is caused by the decrease of the boundary layer thickness with increasing θ, which can be observed from the profiles of the velocity component in the tangential direction (Fig. 20). The large values of the Kolmogorov lengthscale outside of the boundary layer can be explained by the weak turbulence levels, which cause low values of $\{\varepsilon^R\}$ and hence large estimations of η. The profiles at 120^0 (Fig. 3 (e)) suggest that $8C_{kolm}\eta$ is greater than both $\psi\frac{L_{RM}}{10}$ and $\psi\lambda$ at most of the stagnant stratified region apart from the locations where $\psi\frac{L_{RM}}{10}$ and $\psi\lambda$ reach their highest values, which can also be seen from Fig. 8 (a) and Fig. 8 (b).

The pure RANS estimations of the "elliptic blending parameter" α and the "wall-normal anisotropy" $\frac{\langle v^2\rangle}{k}$ are shown in Fig. 10. α is significantly less than 1 not only close to the walls but also in the stratified region at the bottom. This means that the damping of the lengthscales $\psi\frac{L_{RM}}{10}$ and $\psi\lambda$ introduced by ψ is active in the bottom region. This can be understood by looking at (20). The small values of α and $\frac{\langle v^2\rangle}{k}$ allow ψ to be less than 1. Note that ψ was designed to introduce a lengthscale damping only near the wall and not in the laminar zones. However, the fact that $8C_{kolm}\eta$ (which is large in nearly all the laminar zones) is introduced as a third argument in (9) prevents σ^L from becoming 0 in the laminar bottom region even when the lengthscales $\psi\frac{L_{RM}}{10}$ and $\psi\lambda$ are significantly reduced because of the presence of ψ in their definitions.

Fig. 16- Fig. **21** show a comparison of the performance of the different simulations in predicting the mean vertical, horizontal and tangential velocities, mean temperature, total turbulent kinetic energy and the rms of the temperature fluctuations (based on the total temperature variance). Regarding the pure RANS results, the delay of the turbulence transition observed earlier from the velocity and turbulence energy contours is also evident from the temperature profiles shown in Fig. 16. The RANS overestimates the temperatures of the rising plume (this is evident in the 0^0 temperature profile shown in Fig. 16 (a)) because the RANS underestimates the turbulence mixing that occurs between the hot plume and the surrounding colder fluid. This large overestimation of the

temperatures of the rising plume causes an overestimation of the temperatures at the locations between 30^0 and 90^0 (see Fig. 16 (b)-(d)). The velocity profiles (Fig. 18 (b), Fig. 18 (c), Fig. 19 and Fig. 20) reveal that the pure RANS underestimates the size of the outerCBL. The same observation of the thin outerCBL was made earlier from the RANS velocity contours (Fig. 13 (c)).

Regarding the predictions of the rms of the temperature (trms) (Fig. 17), the overprediction of the pure RANS temperature fluctuations at the 0^0 location is caused by the transition delay and the underestimation of the turbulence mixing. This somewhat agrees with the observation of McLeod and Bishop (1988) who probed the temperature at $r = 0.5$ in the 0^0 position and found that situations with more turbulence levels correspond to smaller amplitudes of the temperature fluctuations. With regards to the trms predictions at the other locations, it can be observed that the pure RANS gives wrong predictions of the locations of the local peaks that occur in the QDNS data at about r≈ 0.49 and r≈ 0.625 in the 30^0 and 60^0 radial lines, respectively. These trms peaks are caused by the presence of local peaks in the profiles of the radial temperature gradient (the reason for this is that the temperature variance is produced by temperature gradients) that occur in the recirculating flow regions. Since the RANS underestimates the extent of these regions, it predicts the location of the temperature gradient's local peaks to be closer to the wall of the outer cylinder than what the benchmark QDNS data shows. The total turbulent kinetic energy (TTKE) profiles (Fig. 21) show that at 0^0, the RANS overestimates the levels of the velocity fluctuations in the plume central region (between $r \approx 0.229 \; and \; r \approx 0.649$) but underestimates these levels near the two cylinders. At 30^0 and 60^0, the TTKE is underestimated in the entire boundary layer apart from the region near the outer cylinder at the 60^0 location.

Results of the pure LES default C_k simulation are similar to the pure RANS results in that the pure LES simulation exhibits an overprediction of the temperatures between 0^0 and 60^0 (however, the temperature overprediction of the pure LES default C_k simulation is less severe than that of the pure RANS) and an overprediction of the 0^0 trms. Furthermore, near the outer cylinder, there is a clear overprediction of the TTKE and the total temperature variance, which can be observed from the 30º and 60º profiles of the TTKE and the trms (Fig. 21 (b), Fig. 21 (c), Fig. 17 (b) and Fig. 17 (c), respectively). The tangential velocity profile at 30^0 (Fig. 20 (a)) features an underprediction of the boundary layer thickness, whereas the 60^0 profile (Fig. 20 (b)) gives a reasonable estimation of the boundary layer thickness. The improvement in the prediction of the boundary layer thickness from 30^0 to 60^0 is likely to be due to an error cancellation in which the problem of the underprediction of the boundary layer thickness was cancelled by an overprediction of the wall-normal turbulence mixing of the momentum in the tangential direction.

Concerning the results of the pure LES reduced C_k simulation; the prediction of the 0^0 velocity profile (see Fig. 18 (a)) is reasonable (despite the presence of a slight underprediction of the velocities between $r \approx 0.6 \; and \; r \approx 1$). At the angle of 30^0, the pure LES reduced C_k predictions show some deviation from the QDNS data (see Fig. 18 (b), Fig. 19 (a) and Fig. 20 (a)) and at 60^0 (see Fig. 18 (c), Fig. 19 (b) and Fig. 20 (b)) the deviation becomes much more pronounced as the LES overestimates the thicknesses of the descending flow region (the region with positive tangential velocity values near the outer cylinder) and the boundary layer. On the other hand, the hybrid simulations give much more accurate velocity profiles at both 30^0 and 60^0. The fact that in the hybrid framework the coarse LES is corrected towards the RANS in the near-wall region allows the LES to do a good job in capturing the outer edge of the boundary layer. Indeed, one of the motivations for using hybrid RANS-LES to simulate this flow and the flow reported in Ali et al. (2021) is that compared to the RANS approach, the LES is more capable of capturing the interaction of the large eddies at the outer edge of a turbulent boundary layer with the laminar regions far from the wall as these interactions are resolved in the LES unlike in the RANS, where they are completely modelled. However, admittedly, the hybrid method overpredicts the near-wall peaks of the 60^0 velocity profiles. Nonetheless, it is difficult to obtain accurate predictions of all the near-wall locations as these locations are handled by the RANS. The streamlines estimated from the mean velocities of the pure LES reduced C_k and the hybrid RANS[3] simulations (Fig. 15 (b) and Fig. 15 (d), respectively) show that the two simulations yield different predictions of the size of the recirculating flow regions, which agrees with what was observed from the velocity profiles.

With regards to the total turbulent kinetic energy (TTKE) results returned by the pure LES reduced C_k simulation (Fig. 21), the 0º predictions are in better agreement with the QDNS data near the inner cylinder compared to the predictions of the pure LES default C_k simulation (due to the improved transition prediction in the former). At 60º, the reduced C_k simulation exhibits a significant overprediction of the TTKE. Additionally, the local TTKE peaks (which are located at $r \approx 0.46$ and $r \approx 0.58$ in the 30^0 and 60^0 positions, respectively in the QDNS profiles) are not well captured by the reduced C_k simulation. On the other hand, forcing the coarse LES towards the RANS near the wall (i.e. using the dual-mesh approach) helps to reduce the problem of overpredicting the turbulence

[3] Since the mean velocities of the hybrid LES and the hybrid RANS simulations are consistent, it is expected that both simulations have similar mean velocity streamlines and hence only the hybrid RANS streamlines are shown here.

levels and allows the LES to give a more accurate prediction of the locations of the local peaks of the TTKE (particularly at 60^0). This is because the local peaks are related to the presence of the recirculation regions, whose size is well captured by the hybrid method (as observed earlier from the velocity profiles).

Regarding the mean temperature and trms profiles (Fig. 16 and Fig. 17, respectively), the profiles of the pure LES reduced C_k and the hybrid simulations at 0^0 are satisfactory. Even though at 30^0 and 60^0 the temperature profiles of these simulations seem to be in very good agreement with each other and with the QDNS data, the temperature gradient profiles shown in Fig. 22 reveal that the temperature results of the simulations are not identical. In particular, at 60^0, the pure LES reduced C_k simulation predicts the local peak that occurs in the profile of the hybrid method at $r\approx 0.625$ to be more shifted towards the inner cylinder. As explained previously, the local peaks in the temperature gradient profiles correspond to local peaks in the trms profiles. The fact that the hybrid simulations give more accurate predictions of the values and the locations of the trms local peaks at 30^0 and 60^0 compared to the pure LES reduced C_k simulation means that the hybrid simulations are superior to the pure LES in capturing the temperature gradient's local peaks. Another observation that can be made is that there is a good correspondence between the temperature gradient and the trms profiles in that at locations where the hybrid method gives a higher prediction of the temperature gradient than the pure LES reduced C_k simulation, the hybrid trms is greater than the pure LES reduced C_k trms and vice versa.

The overprediction of the trms and TTKE values of the hybrid and the pure LES reduced C_k simulations near the inner cylinder is caused by the fact that the LES grid is deliberately made coarse in the tangential direction at most of the angular locations in order to prohibit the pure LES from accurately resolving the structures near the outer cylinder. This was done to allow this study to explore whether forcing the coarse LES towards the RANS close to the outer cylinder can improve the LES results. The fact that the Rayleigh number of the flow is low necessitated a significant coarsening of the grid near the outer cylinder. Coarsening the grid in the tangential direction near the outer cylinder resulted in large tangential grid spacings near the inner cylinder since a structured grid is used in this study. However, for high Rayleigh numbers, the grid does not have to be significantly coarse to be under-resolved close to the outer cylinder. Thus, one can design a grid that can resolve the innerCBL accurately and at the same time be under-resolved near the outer cylinder.

5. Conclusions

In this work, the dual-mesh hybrid RANS-LES method was applied to the buoyant flow inside a cylindrical annuli enclosure. This was also accompanied by pure RANS and pure coarse LES studies of the flow. The areas that are characterized by an active flow in the enclosure include the boundary layer over the inner cylinder, the buoyant rising plume (which encounters a laminar-turbulent transition near the inner cylinder) and the turbulent boundary layer over the outer cylinder. The region that is located under the inner cylinder is stably stratified and oscillates slowly under the action of the gravity waves.

The one equation k LES model with its default coefficients was found to be unable to predict the turbulence transition. Similar observations were made about the Smagorinsky model by Miki et al. (1993) and Addad (2004), who obtained better results for the annuli flow by lowering the value of the Smagorinsky constant. In the present study, a better transition prediction was achieved by lowering the constant C_k (which appears in the k_{sgs} equation's production term) at the cells located in the inner cylinder's boundary layer. This was done by running a precursor coarse LES simulation in which the default C_k value was used in the entire domain. This was followed by using the formula in **Error! Reference source not found.** to identify the cells at which C_k needs to be reduced. The reduced C_k values were used in the hybrid LES part of the dual-mesh simulation and in a second pure coarse LES simulation.

The lengthscale resolution criterion of Ali et al. (2021) was used in the dual-mesh simulation for the purpose of automatically determining the locations where the LES simulation is forced towards the RANS and vice versa. An analysis of the behaviour of the different lengthscales used in the definition of this criterion in this flow was presented and can be considered complementary to the analysis that was conducted in Ali et al. (2021) for a buoyant square cavity flow. Additionally, the performance of the dual-mesh approach in predicting the annuli flow was shown to be in general superior to both the pure RANS and the pure coarse LES. This was done by validating the results of the different simulations by comparing their predictions of different quantities relevant to the flow and thermal fields against the QDNS data of Addad et al. (2015). Some qualitative analysis in the form of comparisons of flow contours and streamlines is also presented.

The focus of future studies should be on obtaining high fidelity data for cylindrical annuli flow situations with significant turbulence levels unlike the "weakly turbulent flow" examined here. Two particularly relevant cases are the coaxial cylinders flow at $Ra = 2.38 * 10^{10}$ in an annuli with $R_0/R_i = 3.37$ and the flow at $Ra = 2.38 * 10^{10}$ in an annuli with three internal cylinders. These cases can be found in the LES study of Addad et al. (2006). Acquiring high fidelity data for these flow situations is necessary to further assess the performance of the dual-mesh method in predicting the cylindrical annuli flow. The results obtained in the present study and in Ali et al. (2021) are encouraging and suggest that the dual-mesh approach can be a good candidate for CFD simulations of

buoyancy driven flows. These two studies also serve to further validate the heat transfer extension of the dual-mesh method that was done by Tunstall (2016), who also tested it on a T-junction flow.

Acknowledgments

The authors are thankful to Siemens for funding this work (In particular, Dr Sylvain Lardeau). The authors would also like to thank Dr Ryan Tunstall for providing his well-written dual-mesh code and to Dr Yacine Addad for providing his QDNS data.

References

1. Abed, N., & Afgan, I. (2017). A CFD study of flow quantities and heat transfer by changing a vertical to diameter ratio and horizontal to diameter ratio in inline tube banks using URANS turbulence models. International Communications in Heat and Mass Transfer, 89, 18-30.
2. Abed, N., & Afgan, I. (2020). An extensive review of various technologies for enhancing the thermal and optical performances of parabolic trough collectors. International Journal of Energy Research. 2020, 44 (7), 5117-5164. https://doi.org/10.1002/er.5271.
3. Abed, N., Afgan, I., Iacovides, H., Cioncolini, A., & Nasser, A. (2020a). Assessment and Evaluation of the Thermal Performance of Various Working Fluids in Parabolic trough Collectors of Solar Thermal Power Plants under Non-Uniform Heat Flux Distribution Conditions. Energies, 13 (15), 3776. https://doi.org/10.3390/en13153776.
4. Abed, N., Afgan, I., Cioncolini, A., Nasser, A., & Mekhail, T. (2020b). Thermal performance evaluation of various nanofluids with non-uniform heating for parabolic trough collectors. Case Studies in Thermal Engineering, 22, 100769.
5. Abed, N., Afgan, I., Iacovides, H., Cioncolini, A., Khurshid, I., & Nasser, A. (2021). Thermal-Hydraulic Analysis of Parabolic Trough Collectors Using Straight Conical Strip Inserts with Nanofluids. Nanomaterials 11 (4), 853.
6. Addad, Y. (2004). Large-Eddy Simulations of Bluff Body, Mixed and Natural Convection Turbulent Flows with Unstructured FV Codes. The University of Manchester Institute of Science and Technology.
7. Addad, Y., Gaitonde, U., Laurence, D., & Rolfo, S. (2008). Optimal unstructured meshing for large eddy simulations. ERCOFTAC Series, Quality and Reliability of large-eddy Simulations, vol. 12, Springer, pp. 93–103. https://link.springer.com/content/pdf/10.1007%2F978-1-4020-8578-9.pdf
8. Addad, Y., Rabbitt, M., & Laurence, D. R. (2006). Turbulent Natural Convection in Horizontal Coaxial Cylindrical Enclosures: LES and RANS Models (pp. 507–510). https://doi.org/10.1615/ichmt.2006.turbulheatmasstransf.1050.
9. Addad, Y., Zaidi, I., & Laurence, D. (2015). Quasi-DNS of natural convection flow in a cylindrical annuli with an optimal polyhedral mesh refinement. Computers and Fluids, 118, 44–52. https://doi.org/10.1016/j.compfluid.2015.06.014
10. Afgan, I. (2007). Large eddy simulation of flow over cylindrical bodies using unstructured finite volume methods (Ph.D. thesis), Faculty of Engineering and Physical Sciences, The University of Manchester.
11. Afgan, I., Moulinec, C., & Laurence, D. (2008). Numerical simulation of generic side mirror of a car using large eddy simulation with polyhedral meshes. International journal for numerical methods in fluids, 56 (8), 1107-1113.
12. Ahmed, U., Apsley, D., Stallard, T., Stansby, P., & Afgan, I., (2020). Turbulent length scales and budgets of Reynolds stress-transport for open-channel flows; friction Reynolds numbers (Re_τ) = 150, 400 and 1020. Journal of Hydraulic Research, pp 1-15.
13. Ali, A.E.A. (2020). Dual-mesh hybrid RANS-LES computations of turbulent natural convection flows. University of Manchester.
14. Ali, A. E. A., Afgan, I., Laurence, D., & Revell, A. (2021). A dual-mesh hybrid RANS-LES simulation of the buoyant flow in a differentially heated square cavity with an improved resolution criterion. Computers and Fluids, 224. https://doi.org/10.1016/j.compfluid.2021.104949
15. Andersson, B., Andersson, R., Håkansson, L., Mortensen, M., Sudiyo, R., & Van Wachem, B. (2011). Computational fluid dynamics for engineers.
16. Benhamadouche, S., Afgan, I., & Manceau, R., (2020). Numerical Simulations of Flow and Heat Transfer in a Wall-Bounded Pin Matrix. Flow Turbulence and Combustion, 104 (1), 19-44.

17. Billard, F., & Laurence, D. (2012). A robust k − ε − v 2/k elliptic blending turbulence model applied to near-wall, separated and buoyant flows. International Journal of Heat and Fluid Flow, 33(1), 45–58.
18. Bishop, E. H. (1988). Heat Transfer by Natural Convection of Helium Between Horizontal Isothermal Concentric Cylinders at Cryogenic Temperature. J. Heat Transfer, 110, 109–115.
19. Char, M. I., & Hsu, Y. H. (1998). Comparative analysis of linear and nonlinear low-reynolds-number eddy viscosity models to turbulent natural convection in horizontal cylindrical annuli. Numerical Heat Transfer; Part A: Applications. https://doi.org/10.1080/10407789808913934
20. Craft, T. J., Graham, L. J. W., & Launder, B. E. (1993). Impinging jet studies for turbulence model assessment-II. An examination of the performance of four turbulence models. International Journal of Heat and Mass Transfer, 36(10), 2685–2697. https://doi.org/10.1016/S0017-9310(05)80205-4
21. Davidson, L. (2009). Large Eddy Simulations: How to evaluate resolution. International Journal of Heat and Fluid Flow, 30(5), 1016–1025. https://doi.org/10.1016/j.ijheatfluidflow.2009.06.006
22. Davidson, L. (2019). Non-zonal detached eddy simulation coupled with a steady RANS solver in the wall region. ERCOFTAC Bullentin 89, Special Issue on Current trends in RANS-based scale-resolving simulation methods.
23. de Laage de Meux, B., Audebert, B., Manceau, R., & Perrin, R. (2015). Anisotropic linear forcing for synthetic turbulence generation in large eddy simulation and hybrid RANS/LES modeling. Physics of Fluids, 27. https://doi.org/10.1063/1.4916019
24. Fureby, C., Tabor, G., Weller, H. G., Gosman, A. D., & Tabor,) G. (1997). A comparative study of subgrid scale models in homogeneous isotropic turbulence. Physics of Fluids Physics of Fluids A: Fluid Dynamics, 9(4), 1416–1492. https://doi.org/10.1063/1.858423
25. Germano, M. (1992). Turbulence: the filtering approach. Journal of Fluid Mechanics, 238(1), 325–336. https://doi.org/10.1017/S0022112092001733
26. Guleren, K. M., Afgan, I., & Turan, A. (2010). Predictions of turbulent flow for the impeller of a NASA low-speed centrifugal compressor. Journal of Turbomachinery-Transactions of the ASME, 132 (2)-21005.
27. Han, X., Sagaut, P., Lucor, D., & Afgan, I. (2012). Stochastic response of the laminar flow past a flat plate under uncertain inflow conditions. International Journal of Computational Fluid Dynamics, 26 (2), 101-117.
28. Issa, R. I. (1986). Solution of the implicitly discretised fluid flow equations by operator-splitting. Journal of Computational Physics, 62(1), 40–65. https://doi.org/10.1016/0021-9991(86)90099-9
29. Kahil, Y., Benhamadouche, S., Berrouk, A. S., & Afgan, I., (2019). Simulation of subcritical-Reynolds-number flow around four cylinders in square arrangement configuration using LES. European Journal of Mechanics - B/Fluids, 74, 111-122.
30. Kenjereš, S., & Hanjalić, K. (1995). Prediction of turbulent thermal convection in concentric and eccentric horizontal annuli. International Journal of Heat and Fluid Flow, 16(5), 429–439. https://doi.org/10.1016/0142-727X(95)00051-Q
31. Kuehn, T. H., & Goldstein, R. J. (1978). An Experimental Study of Natural Convection Heat Transfer in Concentric and Eccentric Horizontal Cylindrical Annuli. J. Heat Transfer, 100(4), 635–640.
32. Lardeau, S. (2018). Consistent strain/stress lag eddy-viscosity model for hybrid RANS/LES. Notes on Numerical Fluid Mechanics and Multidisciplinary Design. https://doi.org/10.1007/978-3-319-70031-1_4
33. Launder, B. E., & Sharma, B. I. (1974). Application of the energy-dissipation model of turbulence to the calculation of flow near a spinning disc. Letters in Heat and Mass Transfer, 1(2), 131–137. https://doi.org/10.1016/0094-4548(74)90150-7
34. Lilly, D. K. (1992). A proposed modification of the Germano subgrid-scale closure method. Physics of Fluids A: Fluid Dynamics, 4(3), 633. https://doi.org/10.1063/1.858280
35. McLeod, A. E., & Bishop, E. H. (1989). Turbulent natural convection of gases in horizontal cylindrical annuli at cryogenic temperatures. International Journal of Heat and Mass Transfer, 32(10), 1967–1978. https://doi.org/10.1016/0017-9310(89)90165-8
36. Miki, Y., Fukuda, K., & Taniguchi, N. (1993). Large eddy simulation of turbulent natural convection in concentric horizontal annuli. International Journal of Heat and Fluid Flow, 14(3), 210–216. https://doi.org/10.1016/0142-727X(93)90050-W

37. Mockett, C., Haase, W., & Thiele, F. (2015). Go4hybrid: A European initiative for improved hybrid RANS-LES modelling. Notes on Numerical Fluid Mechanics and Multidisciplinary Design, 130, 299–303. https://doi.org/10.1007/978-3-319-15141-0_24
38. Nguyen, P. T. L., Uribe, J .C., Afgan, I., & Laurence, D. R. (2020). A Dual-Grid Hybrid RANS/LES Model for Under-Resolved Near-Wall Regions and its Application to Heated and Separating Flows. Flow, Turbulence and Combustion, 104, 835–859.
39. Padilla, E. L. M., & Silveira-Neto, A. (2005). Large-eddy simulation of transition to turbulence in a heated annular channel. Comptes Rendus - Mecanique, 333(8), 599–604. https://doi.org/10.1016/j.crme.2005.07.016
40. Revell, A., Afgan, I., Ali, A., Santasmasas, M., Craft, T., de Rosis, A., Holgate, J., Laurence, D., Iyamabo, B., Mole, A., Owen, B., Savoie, M., Skillen, A., Wang, J., & Zhang, X. (2020). Coupled Hybrid RANS-LES Research at the University of Manchester. ERCOFTAC Bulletin. 2020. Vol 120, Pages 67.
41. Sebilleau, F. (2016). Computational Analysis of Buoyancy driven flows across scales. Imperial College of Science, Technology and Medicine.
42. Tunstall, R. (2016). CFD and turbulence modelling for Nuclear Plant Thermal hydraulics systems. University of Manchester.
43. Tunstall, R., Laurence, D., Prosser, R., & Skillen, A. (2017). Towards a generalised dual-mesh hybrid LES/RANS framework with improved consistency. Computers and Fluids, 157, 73–83. https://doi.org/10.1016/j.compfluid.2017.08.002
44. Uribe, J. C., Jarrin, N., Prosser, R., & Laurence, D. (2010). Development of a Two-velocities Hybrid RANS-LES Model and its Application to a Trailing Edge Flow. Flow Turbulence and Combustion, 85, 181–197. https://doi.org/https://doi.org/10.1007/s10494-010-9263-6
45. Van Leer, B. (1974). Towards the ultimate conservative difference scheme. II. Monotonicity and conservation combined in a second-order scheme. Journal of Computational Physics, 14(4), 361–370. https://doi.org/10.1016/0021-9991(74)90019-9
46. Wu, Z., Laurence, D., Iacovides, H., & Afgan, I. (2017a). Direct simulation of conjugate heat transfer of jet in channel crossflow. International Journal of Heat and Mass Transfer, 110, 193-208.
47. Wu, Z., Laurence, D., & Afgan, I. (2017b). Direct numerical simulation of a low momentum round jet in channel crossflow. Nuclear Engineering and Design, 313, 273-284.
48. Wu, Z., Laurence, D., Utyuzhnikov, S., & Afgan, I. (2019). Proper orthogonal decomposition and dynamic mode decomposition of jet in channel crossflow. Nuclear Engineering and Design, 344, 54-68.
49. Xiao, H., & Jenny, P. (2012). A consistent dual-mesh framework for hybrid LES/RANS modeling. Journal of Computational Physics, 231(4), 1848–1865. https://doi.org/10.1016/j.jcp.2011.11.009
50. Xiao, H., Wang, J.-X., & Jenny, P. (2014). Dynamic Evaluation of Mesh Resolution and Its Application in Hybrid LES/RANS Methods. Flow Turbulence Combust, 93(1), 141–170.
51. Xiao, H., Wang, J.-X., & Jenny, P. (2016). An Implicitly Consistent Formulation of a Dual-Mesh Hybrid LES/RANS Method. Commun. Comput. Phys, 1–30.

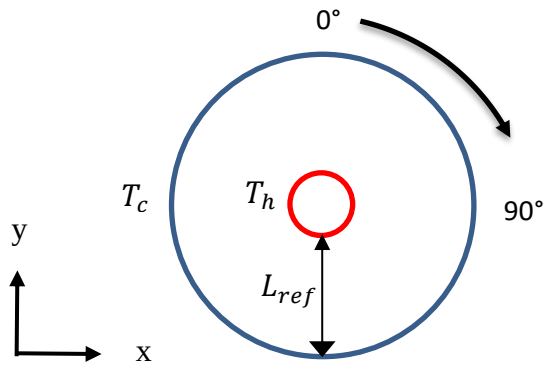

Fig. 1. A schematic of the geometry of the cylindrical annuli.

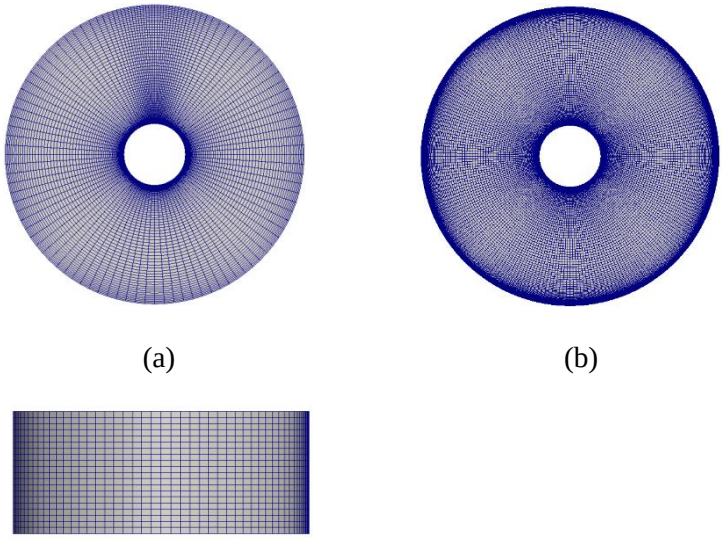

(a) (b)

(c)

Fig. 2. Front (xy) views of the (a) LES mesh (b) RANS mesh. In (c), an xz view of the LES mesh is shown.

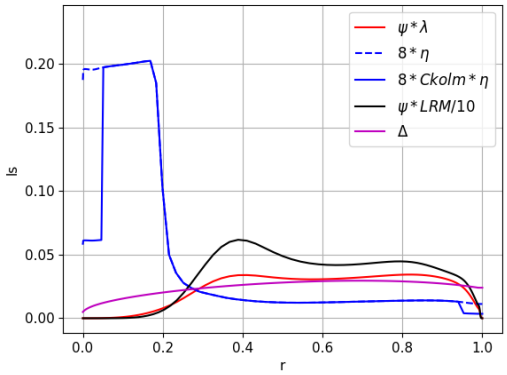

(a)

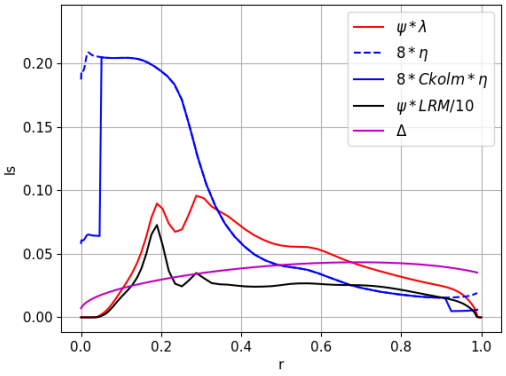

(b)

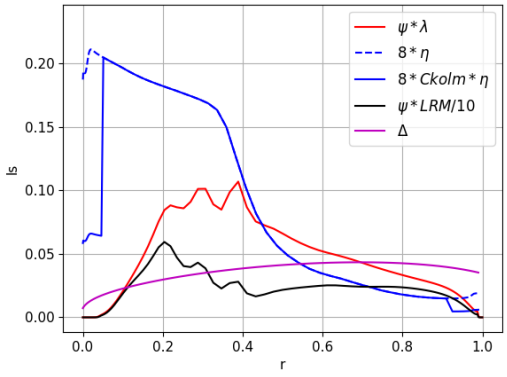

(c)

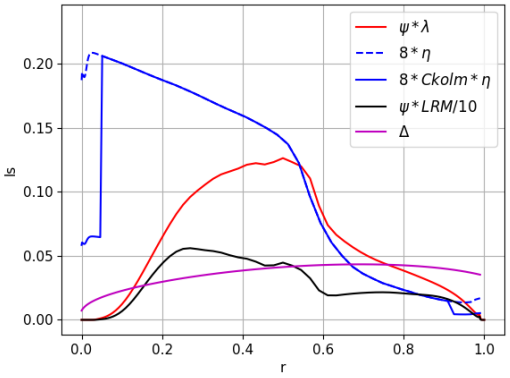

(d)

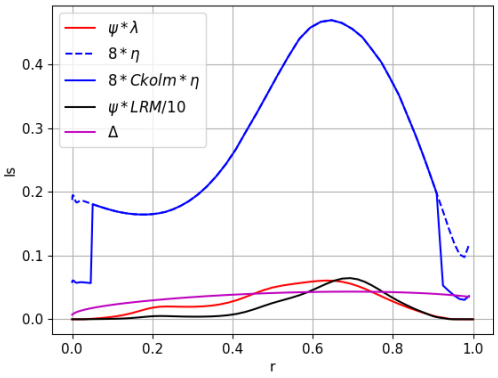

(e)

Fig. 3. Plots showing the behaviour of the lengthscales $\psi\lambda$, $\psi\frac{L_{RM}}{10}$, 8η and $8C_{kolm}\eta$ and the filter width Δ (estimated using $\sqrt[3]{\Delta V}$) at radial lines that correspond to the angular locations of (a) 0° (b) 30° (c) 60° (d) 90° (e) 120°.

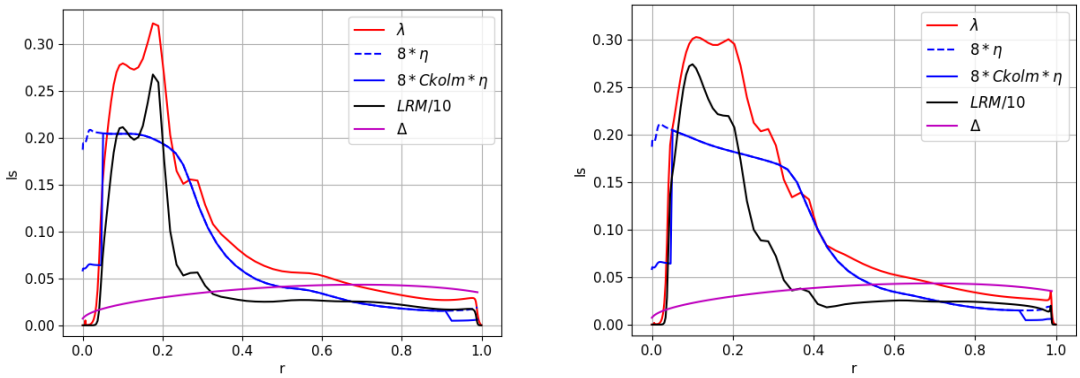

(a) (b)

Fig. 4. Plots showing the behaviour of the lengthscales λ, $\frac{L_{RM}}{10}$, 8η and $8C_{kolm}\eta$ and the filter width Δ (estimated using $\sqrt[3]{\Delta V}$) at radial lines that correspond to the angular locations of (a) 30° (b) 60°.

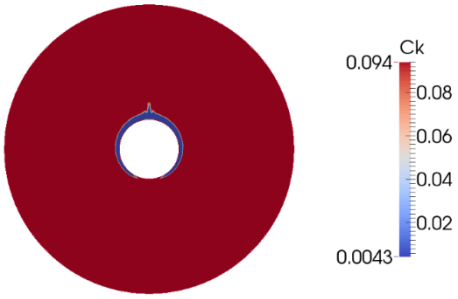

Fig. 5. A contour plot showing how C_k behaves when it is evaluated using (49).

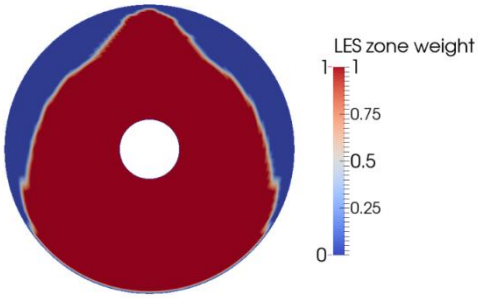

Fig. 6. Contours of the LES zone weight (σ^L) from the dual-mesh simulation. σ^L was calculated using (9).

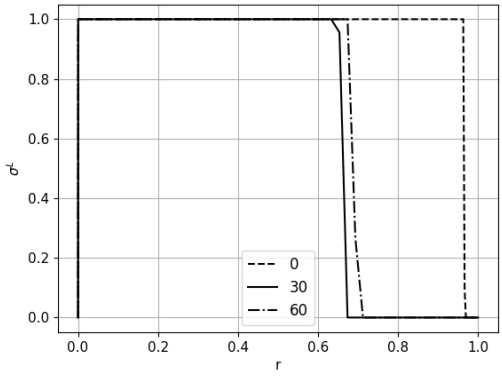

Fig. 7. A plot showing the behaviour of the LES zone weight (σ^L) at radial lines that correspond to the angular locations of 0°, 30° and 60°.

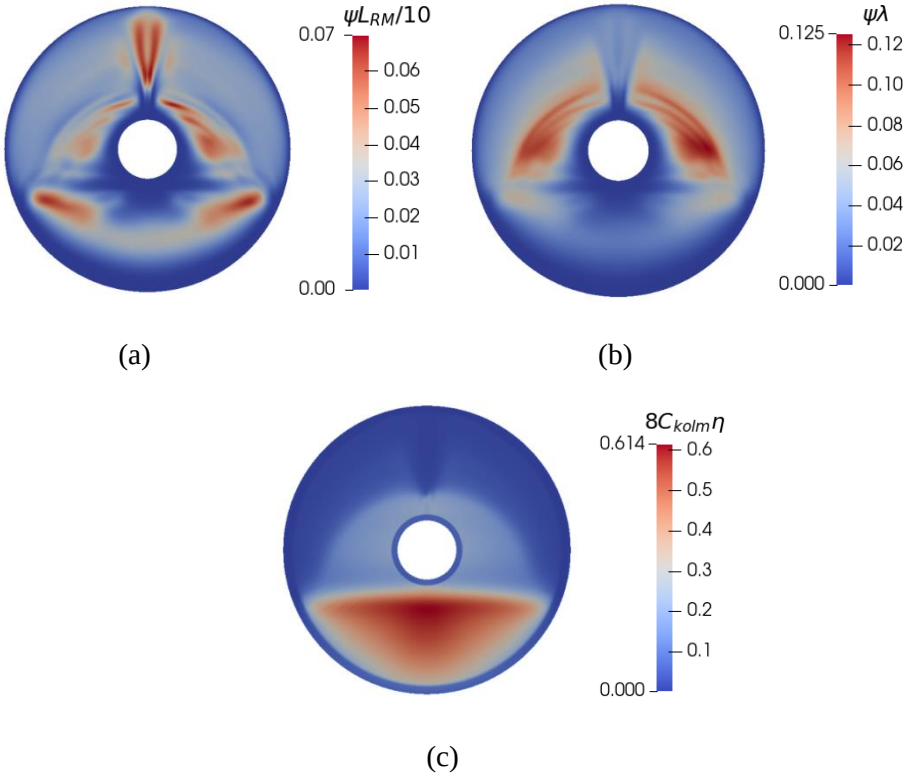

Fig. 8. Contour plots showing the behaviour of the pure RANS estimations of the lengthscales (a) $\psi\frac{L_{RM}}{10}$ (b) $\psi\lambda$ (c) $8C_{kolm}\eta$.

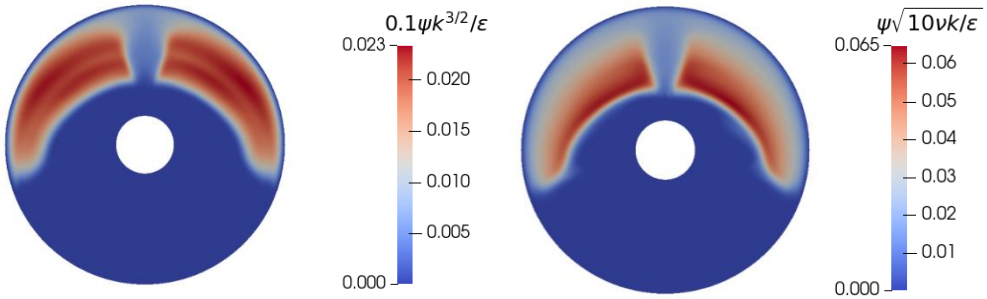

(a) (b)

Fig. 9. Contour plots showing the behaviour of the pure RANS estimations of the lengthscales (a) $\psi \frac{\{k^R\}^{3/2}}{10\{\varepsilon^R\}}$ (b) $\psi\sqrt{\frac{10\nu\{k^R\}}{\{\varepsilon^R\}}}$.

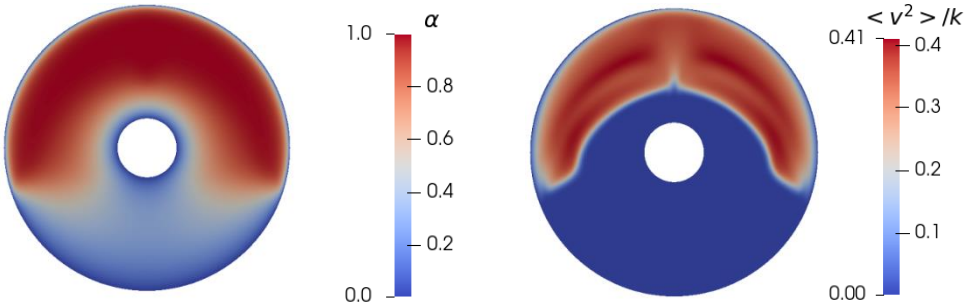

(a) (b)

Fig. 10. Contour plots showing the behaviour of the pure RANS estimations of (a) the "elliptic blending parameter" α (b) the "wall-normal anisotropy" $\frac{\langle v^2 \rangle}{k}$.

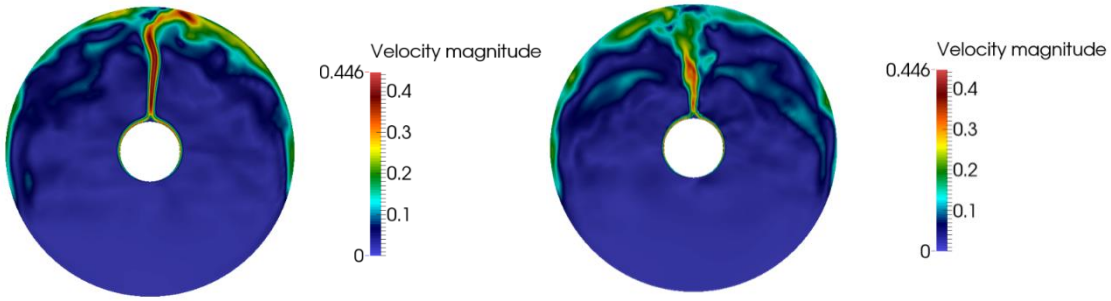

(a) (b)

Fig. 11. Contour plots showing instantaneous snapshots of the velocity magnitude from the (a) pure LES default C_k simulation (b) pure LES reduced C_k simulation.

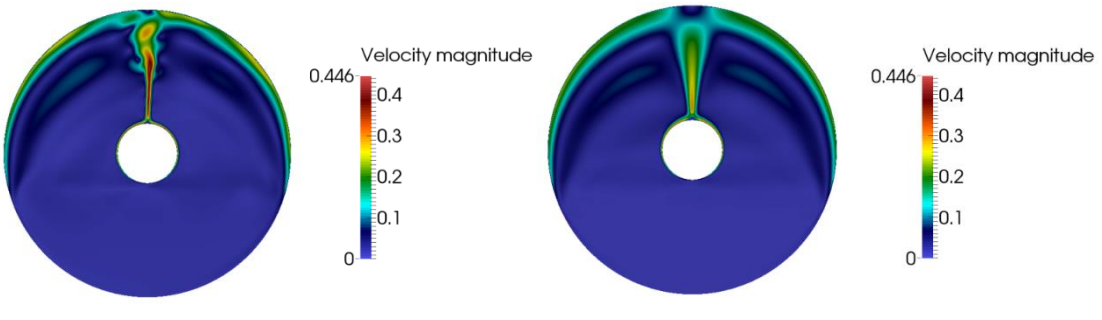

(a) (b)

Fig. 12. Contour plots showing instantaneous snapshots of the velocity magnitude from the (a) pure RANS simulation (b) hybrid RANS simulation.

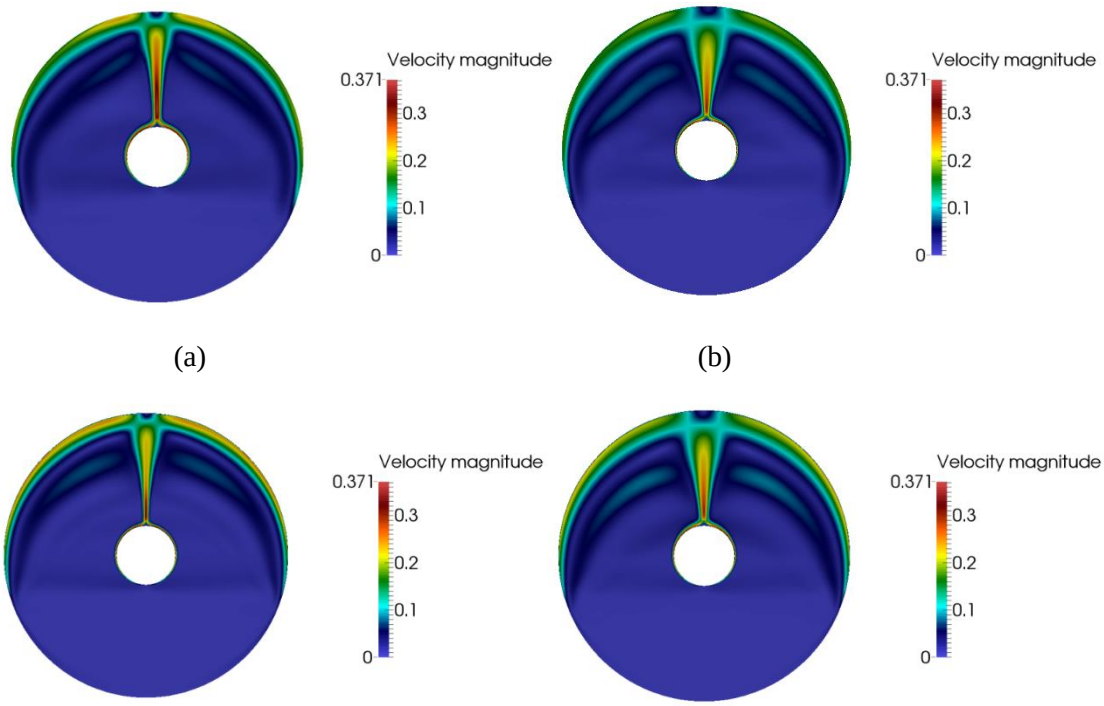

(a) (b)

(c) (d)

Fig. 13. Contours of the magnitude of the time averaged velocity from the (a) pure LES default C_k simulation (b) pure LES reduced C_k simulation (c) pure RANS simulation (d) hybrid RANS simulation.

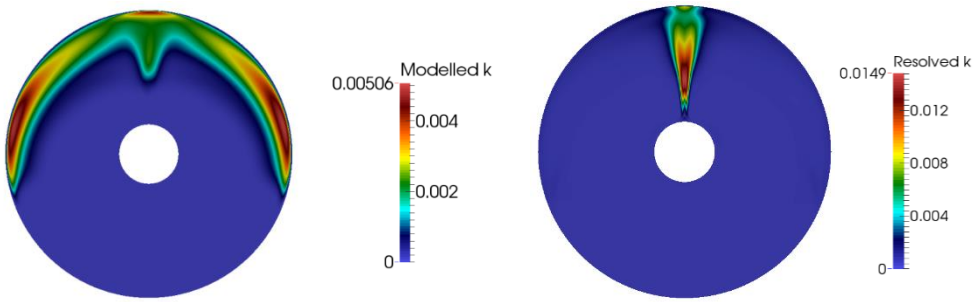

(a) (b)

Fig. 14. Contours of the pure RANS (a) time averaged modelled turbulent kinetic energy (b) kinetic energy of the resolved unsteady motions $\boldsymbol{k^R}_{\boldsymbol{Res}}$, which can be calculated using (16).

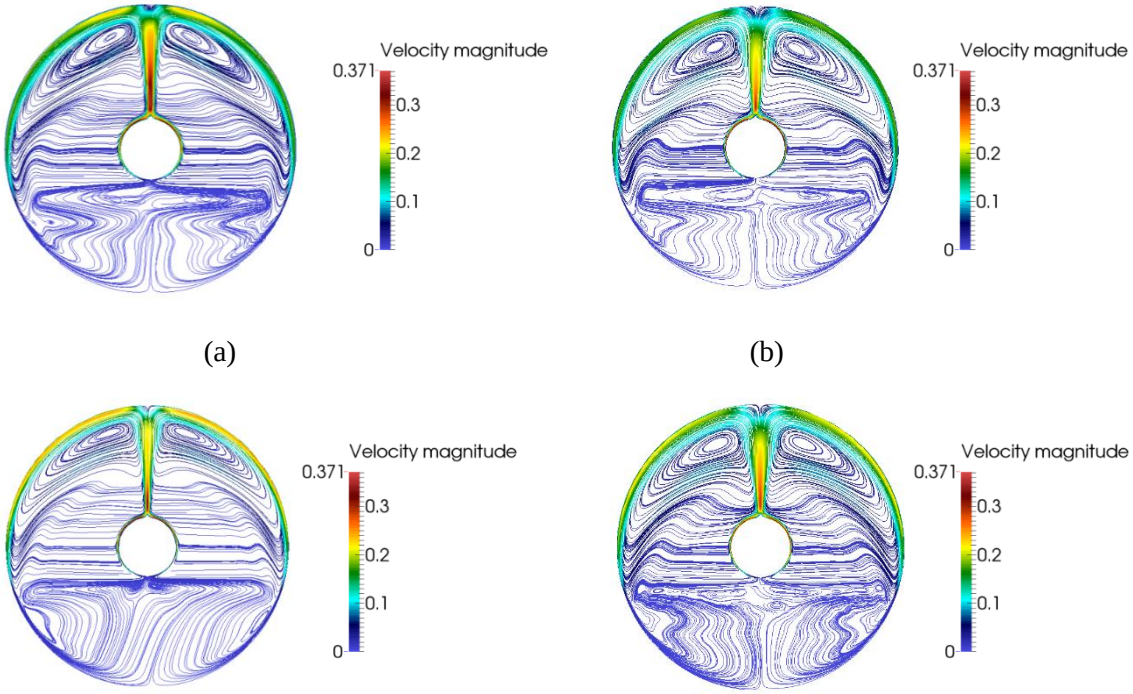

Fig. 15. Mean velocity streamlines predicted by the (a) pure LES default C_k simulation (b) pure LES reduced C_k simulation (c) pure RANS simulation (d) hybrid RANS simulation. The streamlines are coloured by the magnitude of the mean velocity.

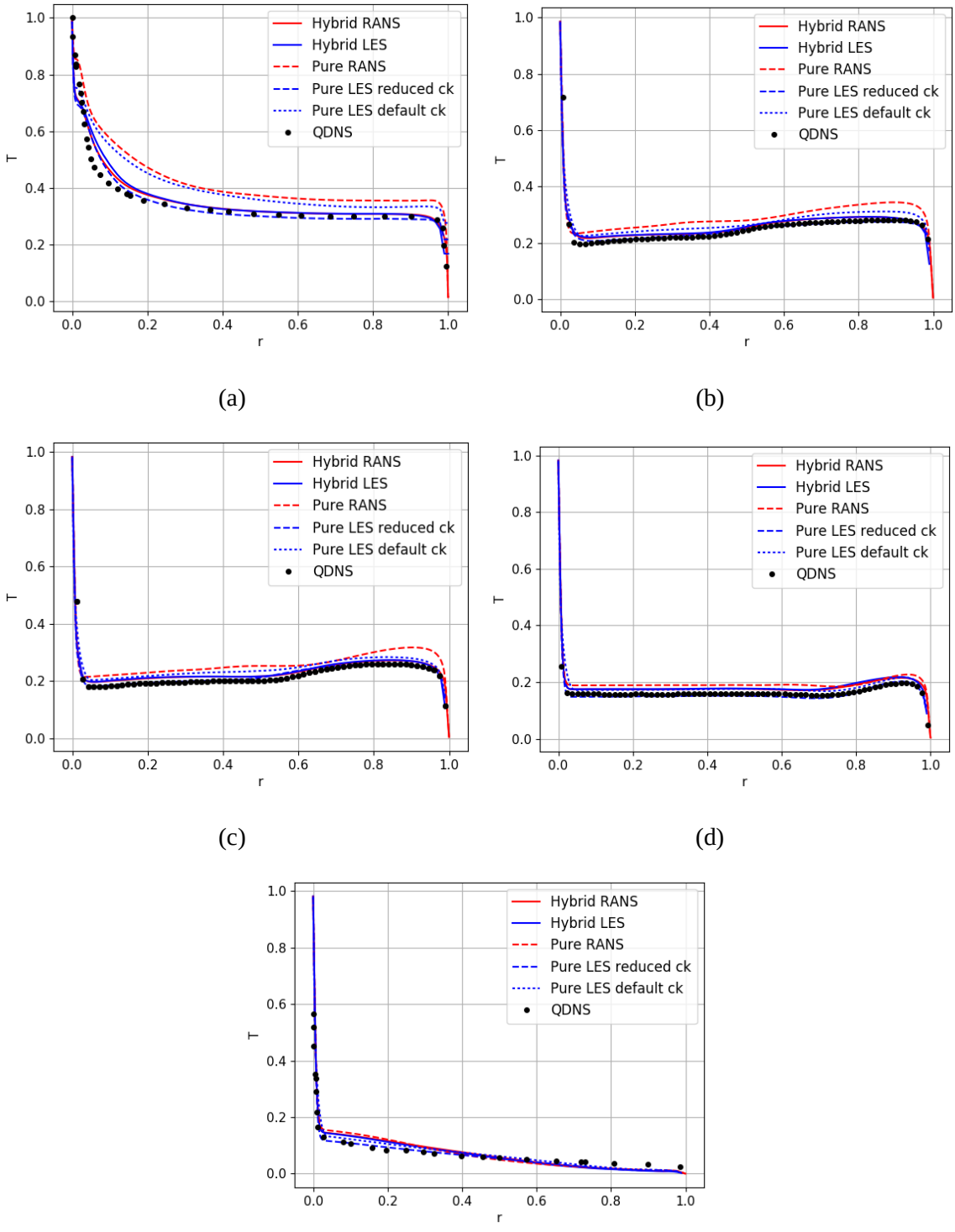

Fig. 16. Mean temperature profiles at radial lines that correspond to the angular locations of (a) 0° (b) 30° (c) 60° (d) 90° (e) 120°.

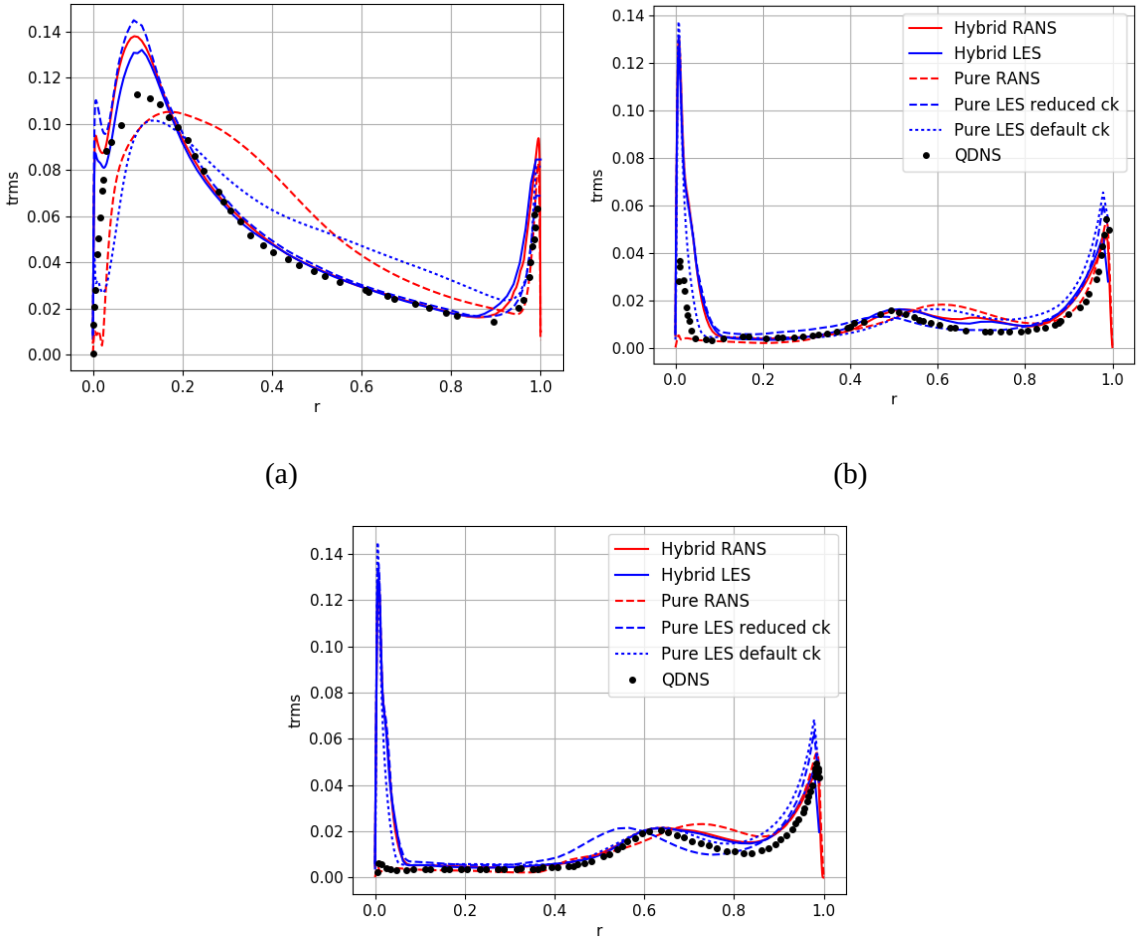

Fig. 17. Profiles of the r.m.s ("root-mean-square") of the temperature fluctuations at radial lines that correspond to the angular locations of (a) 0° (b) 30° (c) 60°.

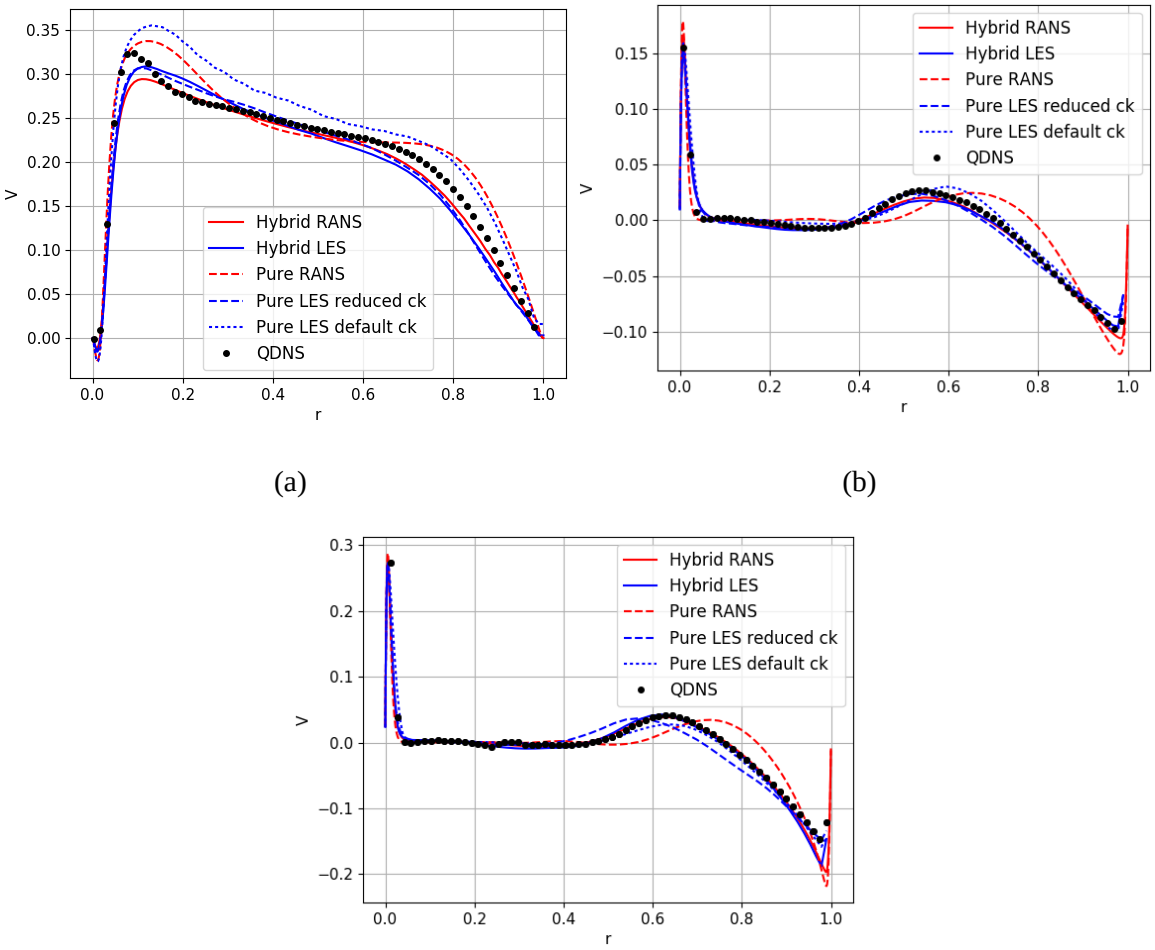

Fig. 18. Profiles of the mean vertical velocity at radial lines that correspond to the angular locations of (a) 0° (b) 30° (c) 60°.

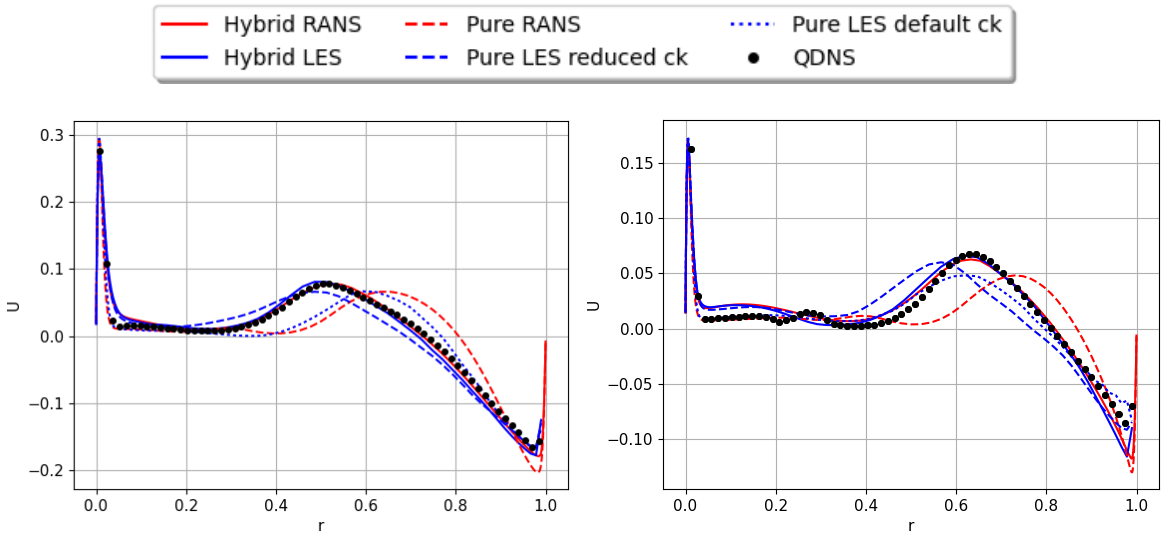

(a) (b)

Fig. 19. Profiles of the mean horizontal velocity at radial lines that correspond to the angular locations of (a) 30° (b) 60°.

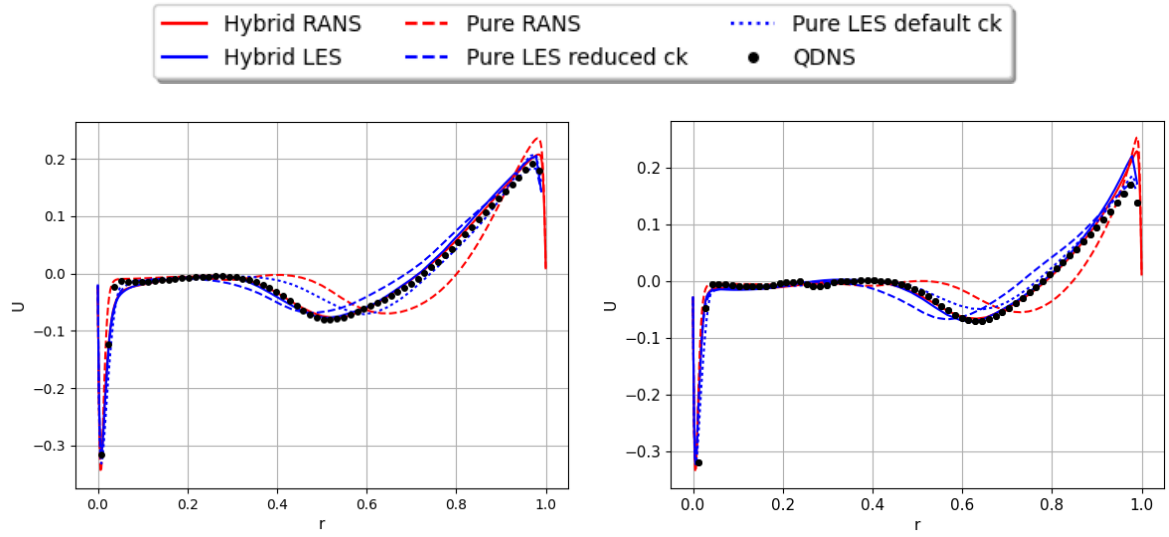

(a) (b)

Fig. 20. Profiles of the mean tangential velocity (the velocity component parallel to the wall) at radial lines that correspond to the angular locations of (a) 30° (b) 60°.

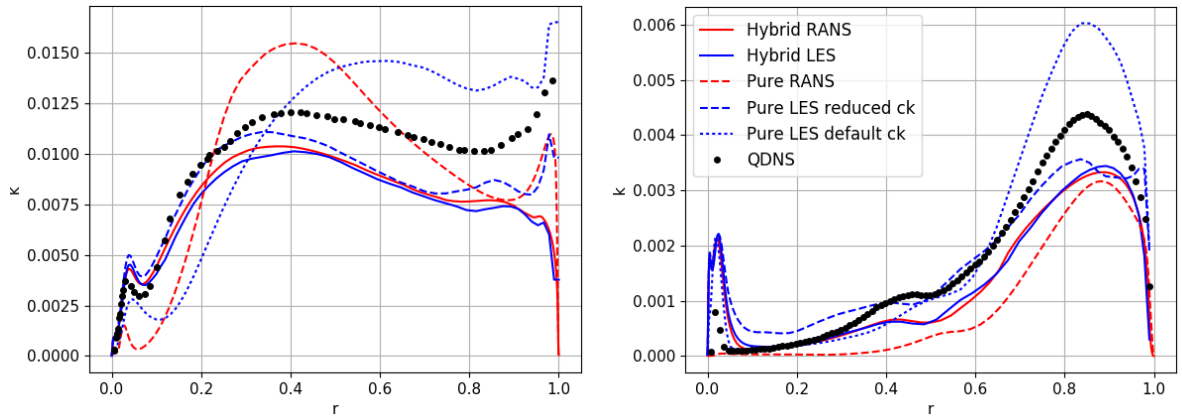

(a) (b)

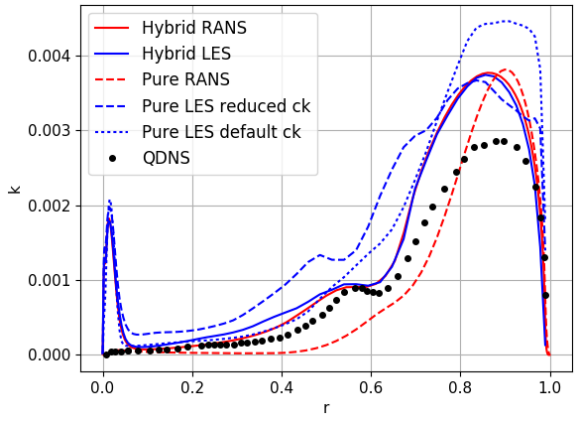

(c)

Fig. 21. Profiles of the total turbulent kinetic energy at radial lines that correspond to the angular locations of (a) 0° (b) 30° (c) 60°.

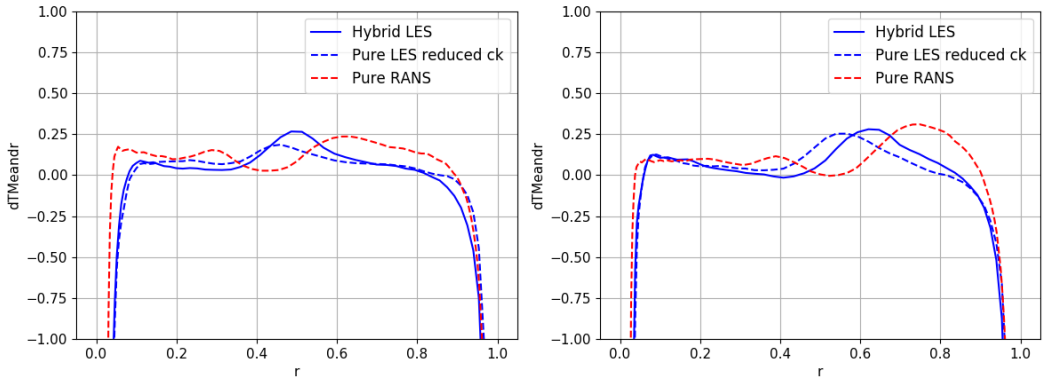

(a) (b)

Fig. 22. Profiles of the radial mean temperature gradient at radial lines that correspond to the angular locations of (a) 30° (b) 60°.